J. Fluid Mech. (1998), *vol.* 361, *pp.* 75–116. Printed in the United Kingdom

Cavitation erosion by single laser-produced bubbles

By A. PHILIPP† AND W. LAUTERBORN‡

Institute of Applied Physics, Technische Hochschule Darmstadt, Germany

(Received 30 August 1996 and in revised form 19 November 1997)

In order to elucidate the mechanism of cavitation erosion, the dynamics of a single laser-generated cavitation bubble in water and the resulting surface damage on a flat metal specimen are investigated in detail. The characteristic effects of bubble dynamics, in particular the formation of a high-speed liquid jet and the emission of shock waves at the moment of collapse are recorded with high-speed photography with framing rates of up to one million frames/s. Damage is observed when the bubble is generated at a distance less than twice its maximum radius from a solid boundary ($\gamma = 2$, where $\gamma = s/R_{max}$, s is the distance between the boundary and the bubble centre at the moment of formation and R_{max} is the maximum bubble radius). The impact of the jet contributes to the damage only at small initial distances ($\gamma \leqslant 0.7$). In this region, the impact velocity rises to 83 m s^{-1}, corresponding to a water hammer pressure of about 0.1 GPa, whereas at $\gamma > 1$, the impact velocity is smaller than 25 m s^{-1}. The largest erosive force is caused by the collapse of a bubble in direct contact with the boundary, where pressures of up to several GPa act on the material surface. Therefore, it is essential for the damaging effect that bubbles are accelerated towards the boundary during the collapse phases due to Bjerknes forces. The bubble touches the boundary at the moment of second collapse when $\gamma < 2$ and at the moment of first collapse when $\gamma < 1$. Indentations on an aluminium specimen are found at the contact locations of the collapsing bubble. In the range $\gamma = 1.7$ to 2, where the bubble collapses mainly down to a single point, one pit below the bubble centre is observed. At $\gamma \leqslant 1.7$, the bubble shape has become toroidal, induced by the jet flow through the bubble centre. Corresponding to the decay of this bubble torus into multiple tiny bubbles each collapsing separately along the circumference of the torus, the observed damage is circular as well. Bubbles in the ranges $\gamma \leqslant 0.3$ and $\gamma = 1.2$ to 1.4 caused the greatest damage. The overall diameter of the damaged area is found to scale with the maximum bubble radius. Owing to the possibility of generating thousands of nearly identical bubbles, the cavitation resistance of even hard steel specimens can be tested.

1. Introduction

The search for the origin of erosion by cavitation bubbles is nearly one hundred years old: it was initiated by the finding of severe destructive effects on the propellers of the great ocean liners *Lusitania* and *Mauretania*, reported first by Silberrad (1912).

† Present address: GAO mbH, Euckenstraße 12, 81369 München, Germany.

‡ Present address: Drittes Physikalisches Institut, Universität Göttingen, Bürgerstraße 42–44, 37073 Göttingen, Germany (to whom correspondence should be addressed).

This was the beginning of investigations of bubble dynamics by numerous researchers all over the world. Since the mechanism of erosion has not been elucidated yet and cavitation erosion still presents a problem, the challenge remains. The mostly unwanted destructive effect appears wherever high pressure gradients or flow rates lead to the generation of bubbles in the vicinity of a solid boundary. It limits the efficiency of hydraulic machinery, like turbines or pumps, and is responsible for lesion of tissue in medical applications of high-intensity ultrasound or lasers, e.g. in the field of ophthalmology (Vogel *et al*. 1990), extracorporeal shock wave lithotripsy (Delius 1990) or laser lithotripsy (Ihler & Hirth 1991).

In order to discover the mechanism of cavitation erosion, in the last three decades bubble dynamics near boundaries has been studied in detail using high-speed photography and acoustic measurements (see review articles by Blake & Gibson 1987 and Steinberg 1993). Two characteristic effects are believed to be mainly responsible for the destructive action: the emission of shock waves upon the collapse of the bubble and the generation of a high-speed liquid jet directed towards the (solid) boundary. A third effect was pointed out by Shutler & Mesler as early as 1965 and its importance will be demonstrated in this paper: during its collapse phase, the bubble is attracted towards the boundary, leading to a reduced distance at the moment of collapse, thereby increasing the damage capability of the shock waves or whatever may be responsible for the damage.

The emission of high-pressure pulses by a collapsing bubble, which originates from a strong compression of the bubble contents, has been well known since the famous theoretical work of Rayleigh (1917) on an imploding spherical cavity. The first experimental evidence of this pressure pulse was given by Harrison (1952) with acoustic measurements and Güth (1954), who was able to visualize the shock wave with a schlieren technique. From precise investigations, including high-speed photography up to a framing rate of one million frames per second and a combined optical and acoustical measurement, Vogel, Lauterborn & Timm (1989) estimated a maximum pressure of 6 GPa inside a bubble which has collapsed down to a minimum radius of 50 μm. Today, the enhanced technology and possibility of producing single bubbles of known size by optimized focusing of a laser pulse (Philipp & Lauterborn 1997), allows the visualization of the collapsing bubble with photography at a framing rate of 20 million frames per second (Ohl, Philipp & Lauterborn 1995). By that, a minimum bubble radius of less than 36 μm was found, demonstrating that the collapse pressure inside the bubble could be even higher.

When a solid boundary perturbs the spherical symmetry, the compression of the bubble contents, and thereby the emitted pressure, is expected to be weaker due to unstable bubble deformations (Benjamin & Ellis 1966). It was shown by Harrison (1952) that a pressure pulse is emitted upon non-spherical collapse, too. Later measurements with single bubbles confirm that even collapse in contact with the boundary is always accompanied by the emission of shock waves (Vogel & Lauterborn 1988; Shima *et al*. 1981), whose pressure amplitudes were estimated to be as high as 1 GPa (Jones & Edwards 1960).

A second consequence of the asymmetry results from the retardation of the fluid flow between the collapsing bubble wall and the boundary. As the pressure in this region is lower than at the opposite bubble wall during the collapse phase, the bubble centre moves towards the boundary. This translational motion is accelerated during the following collapse phases. Therefore, at a certain moment depending on the initial bubble distance from the wall, all subsequent collapses occur in contact with the boundary and consequently the pressure acts with maximum amplitude at the surface.

Motivated by the observation of unstable deformations of the bubble surface during collapse, Kornfeld & Suvorov (1944) suggested another damaging mechanism: the formation of a liquid jet hitting the solid boundary. In the sixties, this jet formation was experimentally confirmed by Naudé & Ellis (1961) and Benjamin & Ellis (1966). Since then, two theories concerning cause of the damage have been discussed: the jet hitting the surface or the shock wave emitted upon collapse of a bubble. As the thin liquid jet reaches very high velocities, its impingement onto a boundary causes high water hammer pressures of short duration. Vogel *et al*. (1989) report a maximum jet impact speed of 100 m s^{-1}, corresponding to a maximum possible water hammer pressure of 450 MPa.

If bubbles erode surfaces by this jet-induced damage mechanism, a single indentation below the centre of the bubble would be expected on a specimen surface. Yet Shutler & Mesler (1965) found indentations around a circumference, centred below the spark which generated the single bubble. The centre itself was undamaged. They further showed by bottom view pictures through a transparent boundary that the bubble shape at minimum volume, i.e. at the moment of collapse, is toroidal. Thus, they concluded that 'the damage is actually caused by the pressure pulse occurring at minimum volume'. The formation of a torus, caused by the jet flow through the bubble centre and radially along the solid boundary, was investigated in detail by Lauterborn and his co-workers (Lauterborn 1982; Vogel *et al*. 1989). By high-speed photography and holography they showed that when the toroidal ring collapses, it divides into several separately collapsing parts. The observation of several shock waves emitted from different locations around the ring is an indication for the development of high-pressure pulses during the collapse of the torus, which could easily explain the circular damage pattern found by Shutler & Mesler.

Tomita & Shima (1986) found a circular pattern as well, but gave a different explanation of the generating mechanism. According to their opinion, tiny bubbles are created when the outward flowing jet along the solid surface collides with the inward moving bubble surface during collapse. At the final stage of collapse, these tiny bubbles would be exposed to the high-pressure pulse emitted by the main bubble and so they may collapse rapidly and consequently multiple impulsive pressure pulses impinge onto the solid surface. As the tiny bubbles are supposed to be generated around a circle of the same size as the observed damage ring, Tomita & Shima were convinced they had found the true damage mechanism.

With the work presented here, an attempt is made to clarify the damage mechanism. As shown by Naudé & Ellis (1961), Tomita & Shima (1986) and Vogel *et al*. (1989), the character and strength of the individual components of the bubble dynamics (jet and its velocity, size of the torus, amount of translational movement towards the boundary) is strongly dependent on the dimensionless distance $\gamma = s/R_{max}$ between bubble and boundary. Thus, if we were able (i) to generate a single bubble with known γ, (ii) to observe its particular dynamics in detail, i.e. its jet velocity and the shape and location of the bubble at any moments of collapse, and (iii) to analyse the damage pattern produced by the bubble on a specimen surface, the damage mechanism could be deduced by varying γ and comparing the varied dynamics with the altered damage pattern.

This idea requires a 'stable single-bubble generator', which is capable of producing single cavitation bubbles of known size at a given moment and distance from a solid boundary. Lauterborn (1974) developed a method called 'optic cavitation' which meets the requirements stated above. He produced single bubbles by focusing a Q-switched laser pulse into water. By the use of well-designed focusing optics we have

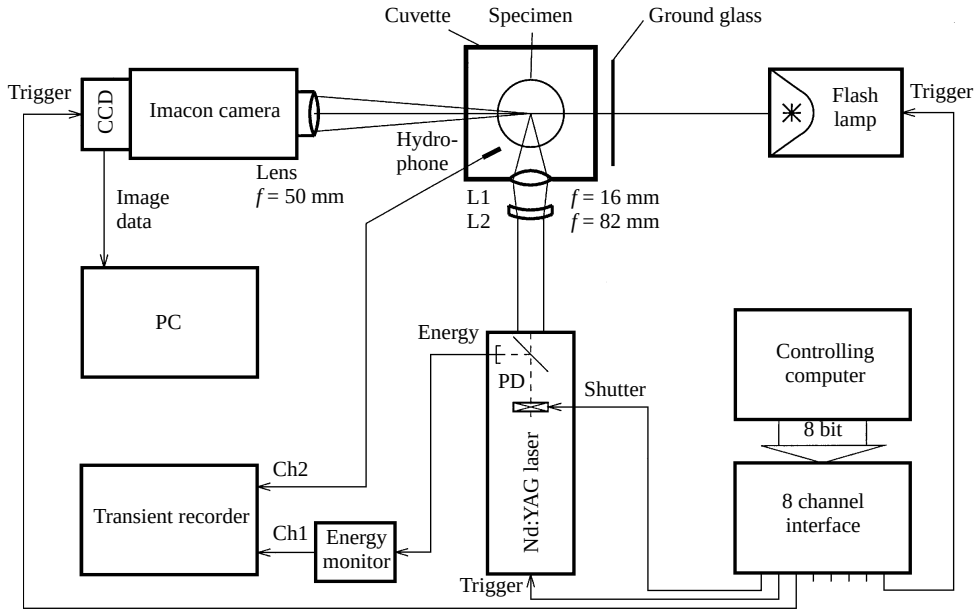

FIGURE 1. Experimental arrangement for investigation of the erosion caused by laser-produced cavitation bubbles.

improved the reproducibility of the bubble parameters. Therefore, we are now able to generate one single bubble with predetermined properties or even hundreds of 'identical bubbles' one after the other.

With this tool, we systematically investigated the dynamics of bubbles in the vicinity of a solid boundary and the resultant erosion pattern for normalized distances in the range from $\gamma = 0$ to 3 in detail. In order to find the effect of the collapse pressure pulses, we determined which of the subsequent collapses take place in contact with the solid boundary. A combination of high-speed photography of bubble dynamics in side and bottom view with a shadowgraph illumination technique allows precise localization of the emission of shock waves during collapse both in time and space and so a correlation with the erosion pattern caused by one single bubble is possible. From picture series with rates of one million frames per second, the jet velocity is determined. Besides the maximum velocity, the impact velocity at the solid boundary is also obtained in order to get knowledge of the water hammer pressure produced by jet impact.

Analysing the specimen surface with interferometric techniques permits three-dimensional measurements of the shallow indentations including quantitative information about their size. The effect of the bubble radius (at constant γ) and the number of successively applied cavitation bubbles on the resulting damage is investigated to complete the picture. Finally, the influence of the material hardness is analysed by experiments with aluminium, brass and various steel specimens.

2. Experiments

To generate a single cavitation bubble, the beam of a Q–switched Nd:YAG laser (Lumonics HY750) is focused into a cuvette filled with doubly distilled water (see figure 1). The laser delivers light pulses with energies up to 740 mJ and a pulse

duration of 8 ns. The focusing optics has been well designed for low aberrations, large cone angle (25.1° in water) and large focal length (26.7 mm) for the sake of high energy concentration and undisturbed bubble dynamics. It consists of two lenses, L1 being an asymmetric biconvex lens (focal length in air $f_L = 16$ mm) and L2 a negative meniscus lens ($f_L = -82$ mm).

The specimen to be investigated (diameter 32 mm) is positioned adjustably below the focus. In order to ensure the detection of even low impact pressures, a very soft material (99.999% pure aluminium) with a highly polished surface was used. Additionally, the erosion strength of materials of different hardness (brass, mild steel and duplex steel) was investigated. Each specimen is exposed to identical bubbles, i.e. with the same size and equal distance to the boundary. Either a single or (successively) up to 5000 bubbles can be generated above eight different positions on the specimen. The laser beam cone is partly cut off at its lower side by the specimen, depending on the distance between the focus and the surface of the specimen. This effect may cause a slightly asymmetric vertical plasma shape, but seems to have minimal effect on the dynamical behaviour of the bubble, as a comparison with spark-produced bubbles (see e.g. Tomita & Shima 1986) reveals. The horizontal plasma shape and consequently the horizontal bubble dynamics are not influenced.

The dynamics of the cavitation bubble is recorded with a high-speed camera (Hadland Photonics, Imacon 700), illuminated diffusely by a Xenon flash lamp through a ground-glass plate. A framing rate of 56 500 frames/s is chosen for overview series and a rate of one million frames/s for fast events like jet formation and shock wave emission. Each series consists of eight pictures which are imaged onto a phosphor screen at the camera back and stored with a slow-scan CCD (Photometrics AT200A). For recording of the shock waves emitted upon collapse, a shadowgraph method was used. For that, the ground glass was replaced by a lens ($f_L = 170$ mm), changing the divergent beam of the flash lamp to a slightly convergent, nearly parallel beam. The pressure gradient across a shock wave deflects the parallel beam rays, thus changing the brightness and the shock wave becomes apparent. In order to get a picture of the three-dimensional structure of the bubble, its dynamics is recorded in side view (the arrangement of figure 1) and, additionally, in bottom-view through a transparent plate, which also serves as the solid boundary. In the bottom-view technique, the optical path for illumination and imaging is deflected by two 45°-mirrors.

The size of the cavitation bubbles is measured indirectly using Rayleigh's formula (Rayleigh 1917)

$$R_{max} = \frac{1}{0.915}\left(\frac{p - p_v}{\varrho}\right)^{1/2} T_{c,\mathrm{Rayleigh}} \tag{2.1}$$

(R_{max} is maximum bubble radius; ϱ, p_v are density and vapour pressure of water, respectively; p is static pressure at infinity). The collapse time $T_{c,\mathrm{Rayleigh}}$ equals half of the duration of the first oscillation cycle of the bubble, i.e. the time interval between generation and first collapse. This interval is determined by measuring the shock waves emitted at optical breakdown and collapse using a hydrophone (Ceram, bandwidth 10 MHz). Now (2.1) is only valid for infinite liquids without boundaries. In the case investigated here of a bubble collapsing in the vicinity of a solid boundary, the oscillation frequency of the bubble is reduced (Strasberg 1953) and therefore, a prolongation of the collapse time must be considered. This prolongation factor, which is dependent on the dimensionless distance $\gamma = s/R_{max}$, was determined experimentally by Vogel & Lauterborn (1988). Its value ranges from 1 to about 1.3; the smaller the distance to the boundary, the longer the collapse phase lasts, as the boundary retards

the fluid flow. Using the measured collapse time T_c and the known distance s, the Rayleigh-collapse time $T_{c,\mathrm{Rayleigh}}$ and hence the maximum bubble radius R_{max} can be deduced with the help of the prolongation factor. As we use smaller γ than investigated by Vogel & Lauterborn (1988) the prolongation factor for $\gamma < 0.5$ has been obtained by extrapolation.

After exposing a specimen to cavitation bubbles, its surface is analysed using interferometric techniques, as the indentations in some cases are very shallow. On the one hand, a microscope with differential-interference contrast (Zeiss Axioplan) is used, where the illuminating beam is divided by a Nomarski prism into two rays having a small displacement. When these two rays are reflected by points on the surface of different height, the phase difference obtained leads to an amplitude contrast after recombination and interference by the prism. Alternatively, quantitative measurements are performed using a phase-shifting microscope (Atos Micromap 512). Its principle of operation is that of a Michelson-interference microscope as constructed by Mirau (see, for example, Tolansky 1973). The specimen surface acts as one of the two mirrors; the second one, the reference mirror, is shiftable by means of a computer-controlled piezo mover. The resulting interference fringes are recorded with a CCD camera and processed by the computer. By shifting the reference mirror successively and recording the different fringe patterns, the phase of a ray reflected by a certain point of the surface, being proportional to its height, can be calculated from the different intensity values of the corresponding CCD pixel (Hariharan, Oreb & Eiju 1987). Thus, the whole three-dimensional structure of the specimen surface is obtained.

3. Results

3.1. *Bubble dynamics*

3.1.1. *Jet formation*

Figure 2 shows the behaviour of equal-sized cavitation bubbles, which were produced at different distances above a solid boundary. The maximum radius achieved during the first oscillation cycle is 1.45 mm at all values of γ. In this and all following high-speed photographs, the direction of the laser beam goes from the right to the left. Each sequence is composed of several series of eight pictures each, and for each of these series, a new bubble was generated. The moment of triggering of recording of each succeeding series was shifted by eight times the interframe time (i.e. $8 \times 17.7\ \mu\mathrm{s} = 142\ \mu\mathrm{s}$ in figure 2). Hence, figure 2(*a*) shows five different parts of the dynamics of five different bubbles but is effectively a continuous sequence in time. But as the reproducibility of bubble generation is good, the recording capacity of the high-speed camera can be extended with this technique. Figures 2(*a*) and 2(*h*) show the bubble dynamics starting from the moment of optical breakdown; all the others start some time before the first collapse, as the first expansion phase shows only marginal changes.

The principal sequence of events during the collapse of a bubble in the vicinity of a solid boundary is illustrated by figure 2(*a*) (see also Benjamin & Ellis 1966 and Vogel *et al*. 1989). At the moment of maximum expansion, the pressure inside the cavitation bubble is much lower than the static ambient pressure, so the bubble starts to collapse. The radial water flow is retarded by the solid boundary (which is located below the bubble and the frames in figure 2*a*). Therefore, the pressure at the lower bubble wall is smaller than the pressure at the upper wall during the

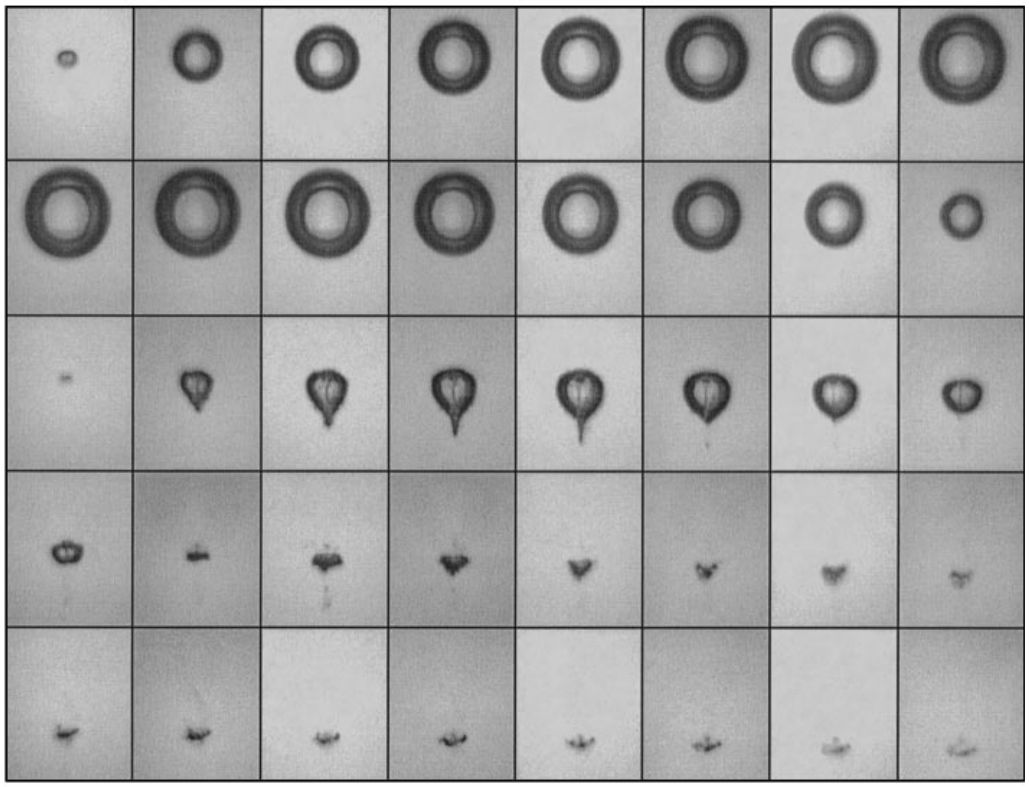

(*a*)

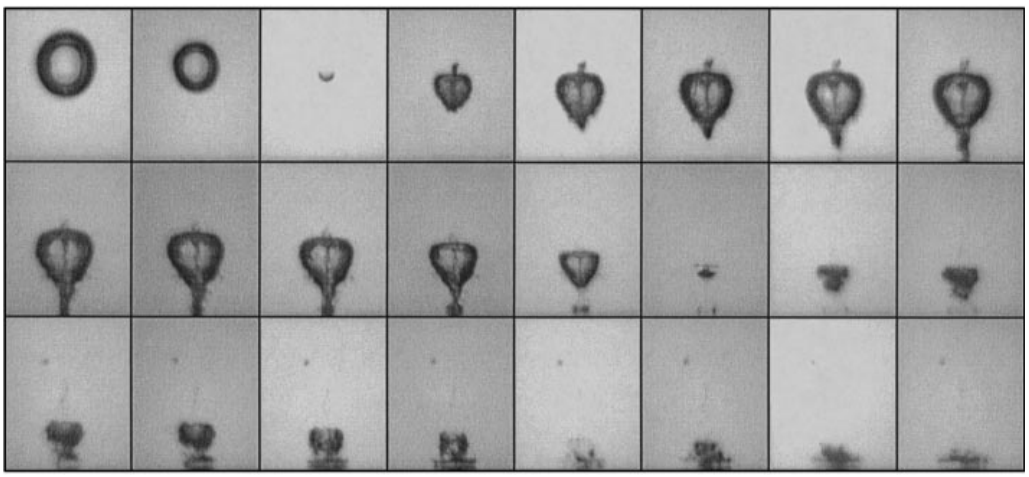

(*b*)

FIGURE 2 (*a,b*). For caption see p. 84.

whole collapse phase (Ward & Emmony 1991*a*) and the bubble becomes elongated perpendicular to the boundary (see e.g. figure 2*d*). The pressure gradient leads to different accelerations of the lower and upper bubble walls and consequently to a movement of the centre of the bubble towards the boundary during collapse. This

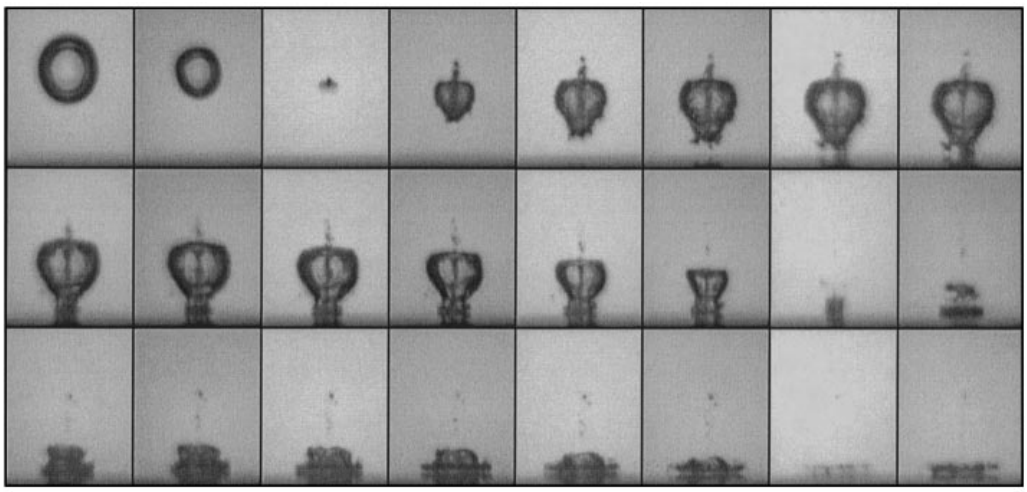

(*c*)

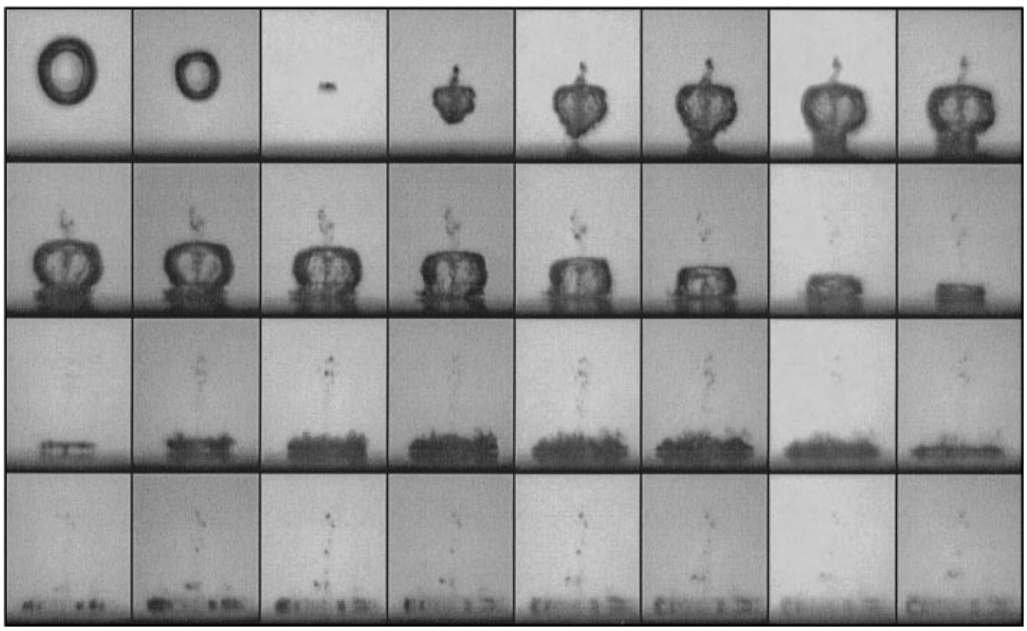

(*d*)

FIGURE 2 (*c*,*d*). For caption see p. 84.

is important since bubbles generated farther away from a boundary may come into contact with it due to this effect. Benjamin & Ellis (1966) pointed out that the 'virtual mass' induced by the fluid flow surrounding the bubble acquires a Kelvin impulse due to the Bjerknes force resulting from the pressure gradient across the bubble. At the end of the collapse cycle, the Kelvin impulse approaches a constant value. Yet, as the impulse is conserved and the virtual mass becomes smaller and smaller during collapse, the velocity of the bubble centre has to increase, i.e. the velocity of the upper bubble wall has to exceed that of the lower wall. Consequently, the fluid volume above the bubble is accelerated and focused during collapse, leading to

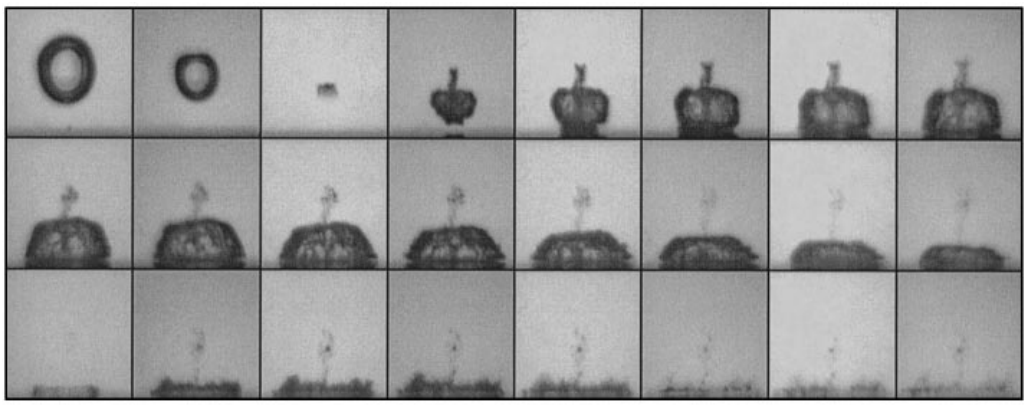

(*e*)

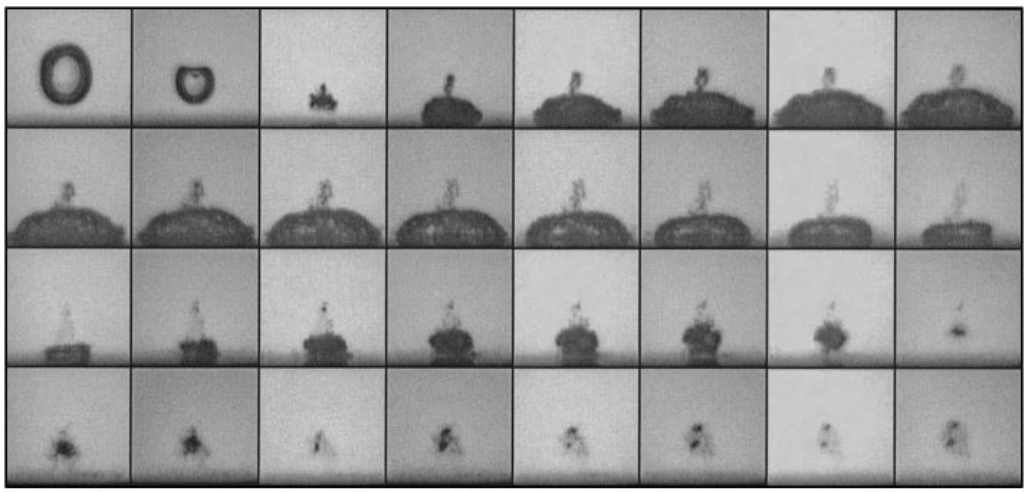

(*f*)

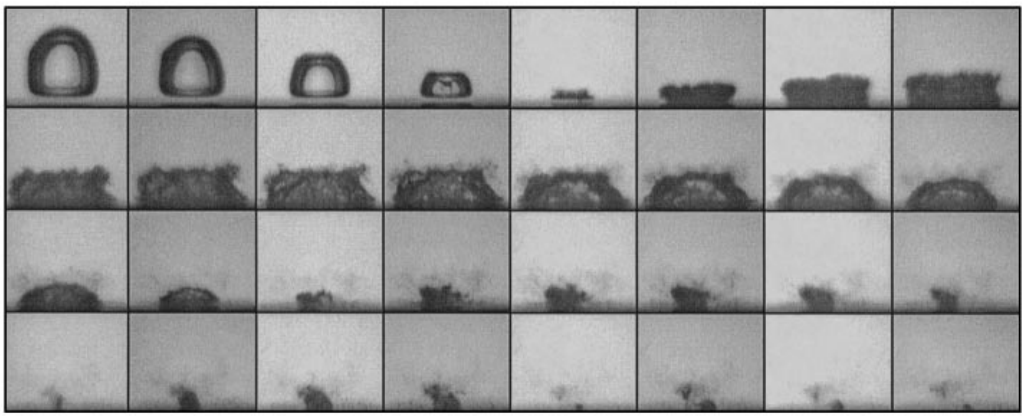

(*g*)

FIGURE 2 (*e*–*g*). For caption see p. 84.

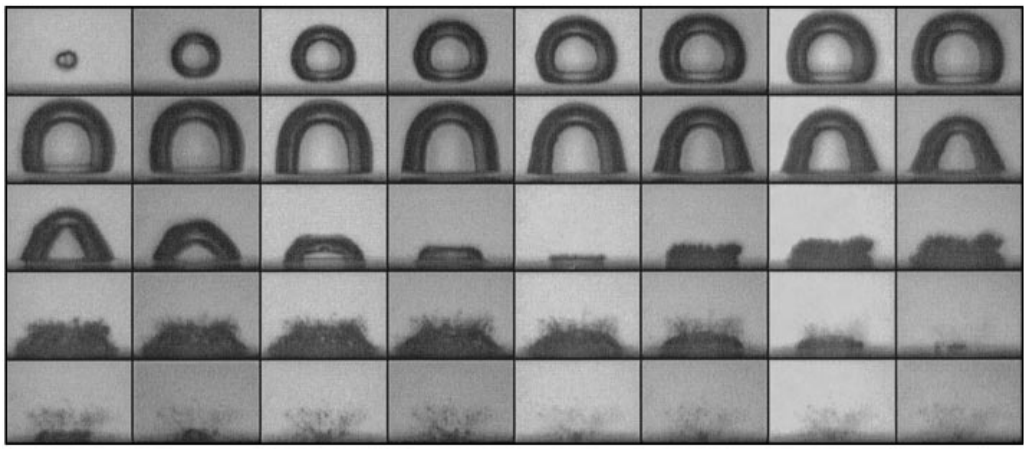

(*h*)

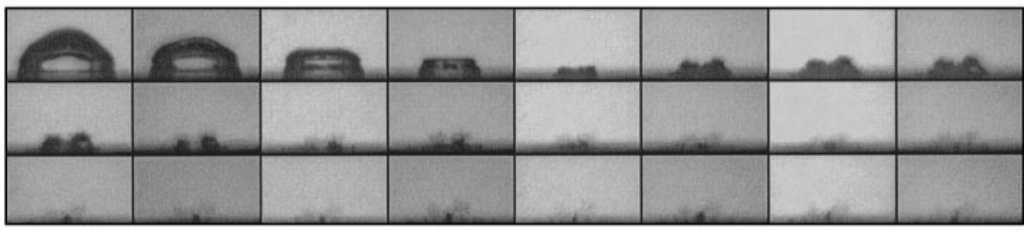

(*i*)

FIGURE 2. Cavitation bubble dynamics in the vicinity of a solid boundary. Each sequence is composed of several time-shifted series of eight frames each (one row). Maximum bubble radius before first collapse $R_{\max} = 1.45$ mm, 56 500 frames/s ($\Delta t = 17.7$ μs), frame width 3.9 mm; (*a*) $\gamma = 3.0$; (*b*) $\gamma = 2.0$; (*c*) $\gamma = 1.8$; (*d*) $\gamma = 1.6$; (*e*) $\gamma = 1.4$; (*f*) $\gamma = 1.2$; (*g*) $\gamma = 0.9$; (*h*) $\gamma = 0.6$; (*i*) $\gamma = 0.3$.

the formation of a liquid jet directed towards the boundary. This jet hits the lower bubble wall, causing a funnel-shaped protrusion (see frames 18 to 21 in figure 2*a*) and finally impacts the solid boundary (frame 8 in figure 2*b*, where the boundary can just be seen at the lower border of the frames). The jet flow through the bubble changes the topology of the cavity: the bubble becomes toroidal. During the second collapse, the combination of the fluid flow towards the bubble and the jet flow through the bubble centre results in the formation of a vortex ring, which conserves the Kelvin impulse by the continued translational movement towards the boundary. The toroidal bubble core of the vortex passes through several expansion and collapse cycles as well, until it finally decays into tiny microbubbles due to instabilities.

When the initial distance is reduced from $\gamma = 3$ to near zero, the basic mechanisms are the same, but the strength and the starting time of the individual components change (see figure 2). Lauterborn (1982) stated that integral quantities (such as, for instance, the Kelvin impulse) are not sufficient to describe the movement of each point on the bubble wall and in the surrounding liquid flow field. As figures 2(*a*) to 2(*i*) show, the behaviour of the bubble shows a rich variety manifested in different structures. Consequently, the erosion forces can be expected to vary in the same manner.

This section focuses on the behaviour and damage capability of the liquid jet. As will be shown, the jet impact velocity on a specimen surface increases when the initial normalized distance γ is reduced. A reduction of γ has two effects: first, the formation of the jet starts earlier with respect to the collapse (compare e.g. figures 3*a* to 3*c*) and secondly, when $\gamma < 1$, the jet hits the solid boundary directly without being decelerated by a water layer, as the lower bubble side is in contact with the boundary from the moment of maximum expansion (figure 2*g*). Thus, the distance parameter range can be divided into three sections showing different jet behaviour as follows.

(i) When γ is greater than about 2.2, the retarding effect of the boundary on the fluid flow during collapse is small. Therefore, the bubble remains nearly spherical and only a small elongation develops in the very late stage of the collapse. According to Lauterborn (1982), jet formation can be explained by differently curved parts of the bubble surface, as the proportional relation between radius and collapse time (Rayleigh's formula) may be adopted for local radii as well. More highly curved parts of the bubble surface collapse faster than less curved parts. The jet is a consequence of a faster liquid flow in the region above the bubble. The small and late appearing elongation at $\gamma = 3.0$ has the effect that only a few moments before collapse a small amount of water in the region above the bubble is accelerated more strongly than at the remaining bubble surface. Therefore, only a thin jet develops (figure 2*a*). The maximum jet velocity v_{max} is reached at the instant of collapse, as the jet is accelerated until that moment due to the elongated, convex bubble surface during the first part of the collapse and, later on, by a geometry effect. This geometry effect has its origin in the focusing of a nearly incompressible volume of liquid into a region which becomes smaller and smaller. Not more than a fraction of a microsecond before collapse, the jet hits the lower bubble wall (figure 3*a*, $\gamma = 2.5$). The relative velocity between jet and bubble wall is very high (more than 200 s^{-1} in the case of figure 3*a*), but nevertheless, the liquid flow in the opposite direction to the jet acts for only a very short time and the jet is hardly slowed down. At the rebound, the jet pushes the lower bubble wall downwards. As the water layer between bubble and solid boundary decelerates the jet, the impact velocity at the boundary (v_{imp}) is smaller than v_{max}.

(ii) In the range of $\gamma = 1$ to 2.2, the more pronounced influence of the boundary causes a greater elongation and, thus, an earlier start of jet formation (figure 3*b,c*). The jet tip hits the lower bubble wall some time before the moment of collapse: at $\gamma = 1.6$, the protrusion of the lower bubble wall is visible about 1 μs (figure 3*b*, frame 7), at $\gamma = 1.2$ about 5 μs before collapse (figure 3*c*, frame 21). Owing to the flow of liquid in the opposite direction, the jet tip is retarded and whirled, producing bands of tiny bubbles below the collapsed main bubble (figure 3*c*, frame 21). At $\gamma = 1.2$, the jet impacts the solid boundary about 11 μs after collapse (figure 3*c*, frame 32). The impact velocity v_{imp} again is lower than v_{max} owing to the water layer, but of course this retarding effect decreases with decreasing γ.

(iii) When the distance between the location of bubble generation and the solid boundary is smaller than R_{max}, i.e. $\gamma < 1$, the bubble wall touches the boundary at maximum expansion. Therefore, water cannot flow from directly below into the collapsing volume and the bubble remains in contact with the boundary (figures 2*g* to 2*i*). The jet impacts the boundary with maximum speed, without being decelerated by a water layer. Jet formation starts very early; in the case of $\gamma = 0.7$, the tip of the jet is visible as soon as about 35 μs before the moment of collapse (figure 3*d*, frame 1). The main accelerating mechanism at $\gamma < 1$ is the involution of the highly curved upper bubble wall (see e.g. figure 2*h*). The inwardly directed flow into a volume becoming smaller and smaller accelerates the bubble surface as long as it is curved

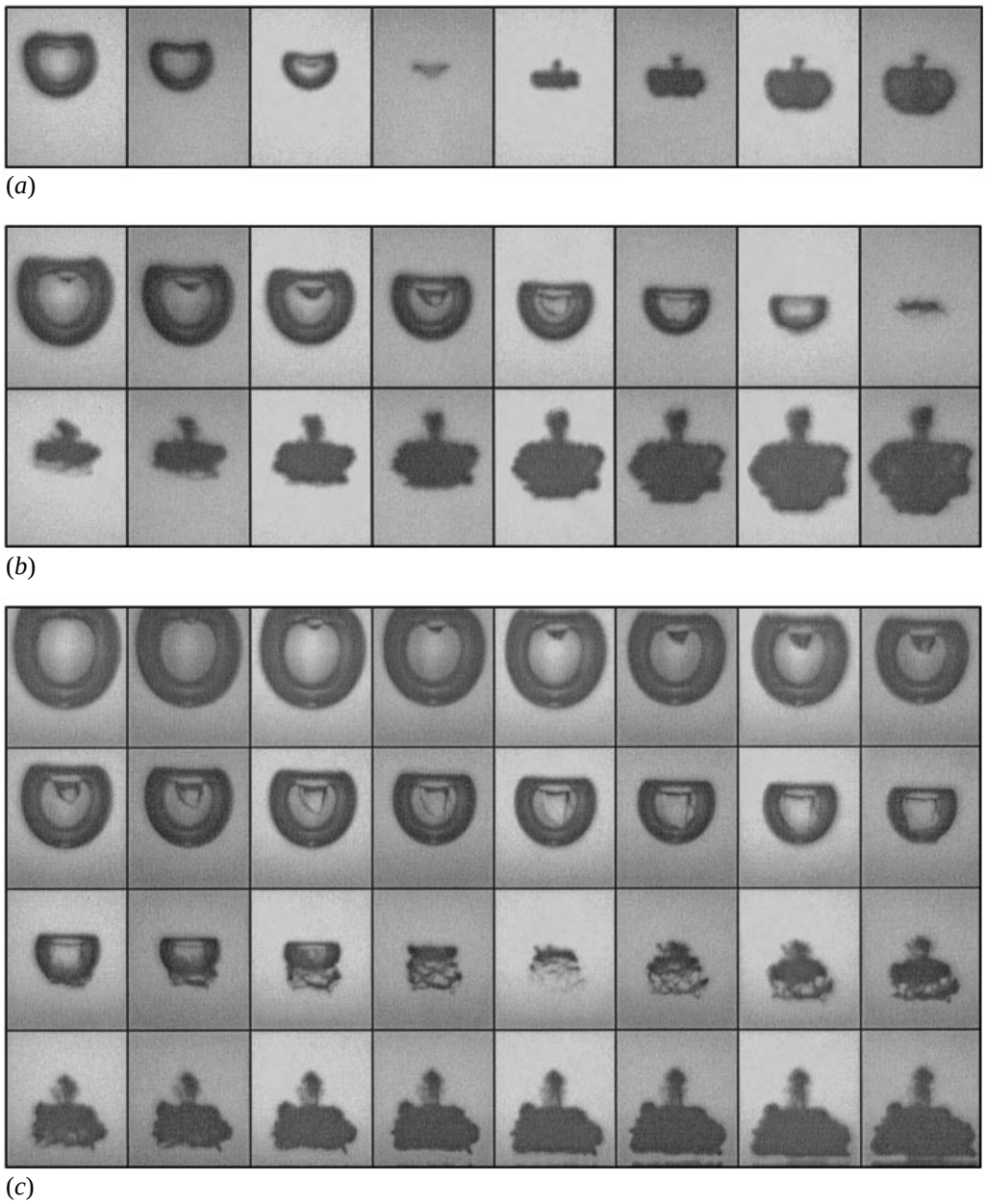

(*a*)

(*b*)

(*c*)

FIGURE 3 (*a–c*). For caption see facing page.

convexly (Vogel *et al*. 1989). From the moment, at which the jet tip is visible inside the bubble, the jet velocity remains nearly constant. This temporal development of the velocity is in good agreement with calculations of Plesset & Chapman (1971). The geometrical effect, which may further accelerate the jet at the end of the collapse cycle, hardly affects the jet tip velocity, as the jet impacts a long time before the moment of collapse (about 26 μs at $\gamma = 0.7$, frame 10 of figure 3*d*). Until collapse, the

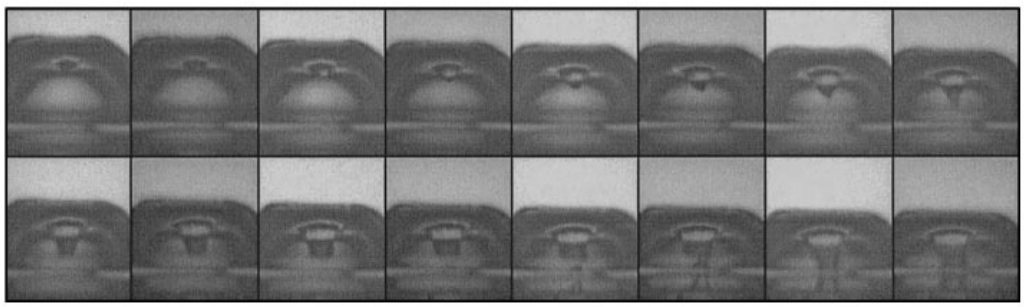

(*d*)

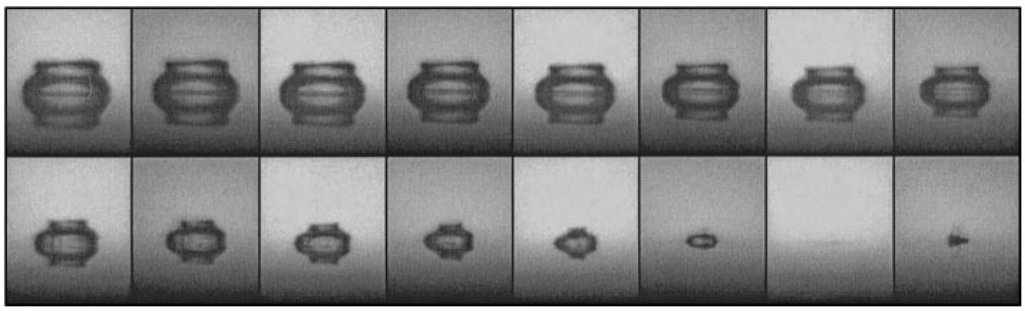

(*e*)

FIGURE 3. Jet formation at different initial distances of a cavitation bubble from a solid boundary. $R_{max} = 1.45$ mm, 10^6 frames/s. Time-shifted combination of several series of eight frames each; (*a*) $\gamma = 2.5$, frame width 1.2 mm; (*b*) $\gamma = 1.6$, frame width 1.2 mm; (*c*) $\gamma = 1.2$, frame width 1.5 mm; (*d*) $\gamma = 0.7$, frame width 1.5 mm; (*e*) $\gamma = 0.1$, frame width 1.5 mm, reflection of the bubble at the polished surface yields the symmetric picture.

jet diameter becomes larger and larger causing a compression of the bubble volume from inside (see § 3.1.2).

Figure 4 shows the relative positions of the upper and lower bubble walls and of the jet tip inside the bubble versus time as obtained from figure 3(*b*). The jet tip position was determined taking into account the imaging through the curved bubble–liquid interface, which acts as a divergent lens. Objects (for example the jet inside the bubbles in figure 3) and distances inside an empty bubble appear smaller by a factor which is equal to the refractive index of the liquid. Hence, the measured distances of the jet tip to the bubble centre are multiplied by 1.33 to give the positions plotted in figure 4. Inside the bubble, the velocity of the jet tip is nearly constant (about 100 m s^{-1}), until the tip collides with the upwardly collapsing lower bubble wall and is briefly retarded thereby. After collapse, the focused liquid flow from the region above the bubble accelerates the jet tip again. The maximum jet velocity, averaged over 2 μs from the moment of collapse, is $v_{\max} = 114$ m s^{-1} (± 8 m s^{-1}) in this example ($\gamma = 1.6$).

The maximum jet velocity becomes slightly smaller when γ is reduced, as the jet hits the liquid interface earlier with smaller γ (see figure 5). Accordingly, the highest velocity was measured at $\gamma = 3.0$ as 138 m s^{-1}. Clearly visible is the increasing velocity for $\gamma < 1$, where the retarding effect due to the collision with the lower bubble wall vanishes. Since the elongation becomes weaker for $\gamma < 0.6$ (figure 2*i*), v_{max} decreases again in this region. A different symbol was chosen at $\gamma = 0.1$ in figure 5. At those small distances, no jet could be observed inside the bubble. Nevertheless, the bubble

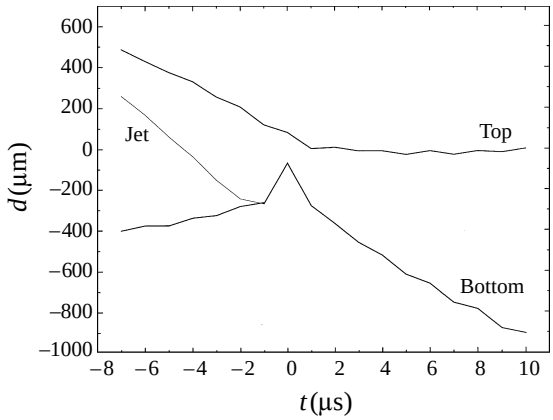

FIGURE 4. Temporal development of the positions of the lower and upper bubble wall and the jet tip of the bubble shown in figure 3(*b*); $R_{max} = 1.45$ mm, $\gamma = 1.6$.

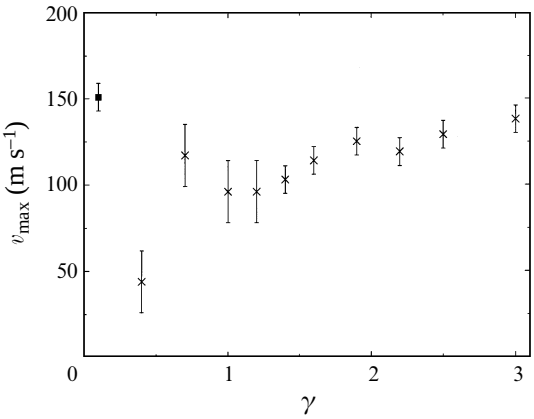

FIGURE 5. Maximum jet velocity, $R_{max} = 1.45$ mm.

collapses very rapidly and the upper bubble wall impacts with a speed of 151 m s^{-1} onto the solid boundary in this case.

For the estimation of the damage capability of the jet, the impact velocity v_{imp} onto the solid boundary is decisive (figure 6). As expected, v_{imp} becomes smaller with increasing initial distance in the parameter range $\gamma \geqslant 1$ due to the increasing thickness of the water layer between bubble and boundary. For $\gamma \geqslant 1.2$, the impact velocity is as low as or even smaller than 25 m s^{-1}. Moreover, in the case of very large distances ($\gamma > 2.5$), the jet flow disintegrates on its way to the boundary (see figure 2*a*), so that jet-induced damage is unlikely. When $\gamma \leqslant 1$ and no water layer cushions the jet flow, the impact velocity reaches 83 m s^{-1} ($\gamma = 0.7$). Again, the square symbol at $\gamma = 0.1$ represents v_{imp} of the upper bubble wall.

The jet velocities presented here are in good agreement with previously published values. Benjamin & Ellis (1966) and Gibson (1968) calculated maximum jet velocities of 175 m s^{-1} and 160 m s^{-1}, respectively, from measurements at reduced pressure. Lauterborn (1974) reports jet velocities of 100 to 200 m s^{-1} at normal pressures, measured from high-speed photographic series at a framing rate of 900 000 frames per second. He assumed that even higher values could be obtained, if faster cameras

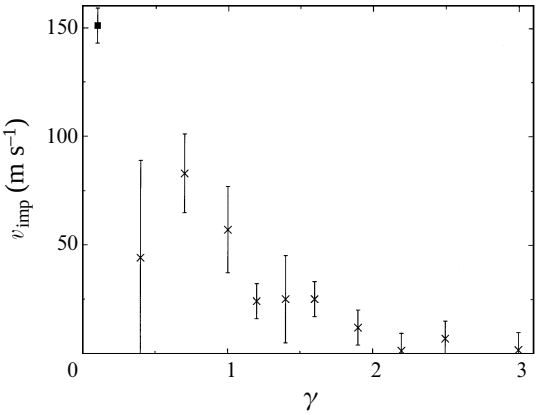

FIGURE 6. Jet velocity at the impact onto the solid boundary, $R_{max} = 1.45$ mm.

were used. Later measurements by different investigators, however, gave no increased values: 120 m s^{-1} (Lauterborn & Bolle 1975), 170 m s^{-1} (Shima *et al*. 1981) or 156 m s^{-1} (Vogel *et al*. 1989), for instance. Even different theoretical models, which exclude the disturbing influences given in real arrangements, show similar results (Plesset & Chapman 1971: 170 m s^{-1}, Blake, Taib & Doherty 1986: 161 m s^{-1}, Zhang, Duncan & Chahine 1993: 120 m s^{-1}). The value of 138 m s^{-1} presented in this work confirms that the maximum velocity of a boundary-induced jet is lower than 200 m s^{-1} at normal pressure. The behaviour of an increased impact velocity at reduced distances was reported by Kling & Hammitt (1972) as well (from 35 m s^{-1} to 120 m s^{-1} when decreasing γ from 1.4 to 1.1), although their values are higher than those presented here (in figure 6: from 25 m s^{-1} to 57 m s^{-1}). The observation of a maximum of v_{imp} in the range of $\gamma < 1$ agrees well with measurements of Tomita & Shima (1986, 130 m s^{-1} at $\gamma = 0.9$) and Gibson (1968, $\approx$ 160 m s^{-1} at $\gamma = 0.6$).

3.1.2. *Bubble collapse at a solid boundary*

The potential importance of the collapse for cavitation erosion is founded on the severe pressure generated inside the bubble, giving rise to the emission of shock waves upon collapse. The pressure amplitude is determined (assuming adiabatic compression) by the relation of maximum to minimum bubble volume (Rayleigh 1917; Fujikawa & Akamatsu 1980). The collapse of a bubble has to be considered as an erosion mechanism if it takes place in contact with the solid boundary. Yet, not only bubbles which arise very close to the boundary may cause damage, but also bubbles which have formed further away because of the translational movement to the surface during the collapse cycles. Thus, the third collapse takes place in contact with the boundary when γ is less than or equal to 2.0, the second from about $\gamma \leqslant 1.9$ and the first from $\gamma \leqslant 0.9$ (see figure 2, the solid boundary is visible at the lower limit of the frames in the figures 2*b* to 2*i*).

The first collapse of a bubble proceeds almost spherically when the normalized distance is large (see figure 2*a*, $\gamma = 3.0$). Owing to the violent collapse, a shock wave of high amplitude is emitted (see e.g. Vogel & Lauterborn 1988 and references therein). However, as the distance of the emission centre from the boundary is large, the pressure acting on the material surface is relatively low. When γ is reduced, the bubble becomes flatter upon collapse due to the jet involution and the shock wave emission becomes more involved.

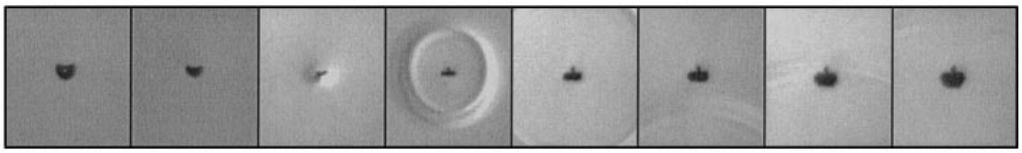

FIGURE 7. First collapse of a bubble in the neighbourhood of a solid boundary. The boundary is located just below the lower limit of the frames; $R_{max} = 1.45$ mm, $\gamma = 2.2$, 10^6 frames/s, frame width 4.0 mm.

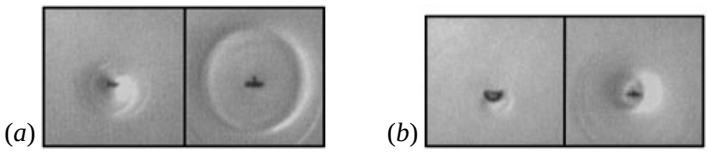

FIGURE 8. Emission of two shock waves during first collapse: (*a*) $\gamma = 1.9$; (*b*) $\gamma = 1.7$, frame width 4.0 mm.

In order to visualize the emitted shock waves which are indicators of impulsive high-pressure regions, high-speed photographic series are taken using the shadowgraph method. Figure 7 shows the emission of two shock waves upon the first collapse of a bubble with $\gamma = 2.2$. From the diameter of the shock waves and their vertical shift, the distance of the centres ($\Delta x = 170$ μm) as well as the time interval between the emissions ($\Delta t = 115$ ns) can be calculated. The first shock wave is generated by the impact of the jet tip onto the lower bubble wall (jet shock wave). From figure 3(*a*), the relative velocity between jet and bubble wall is estimated to be about 220 m s^{-1}, corresponding to a water hammer pressure of about 170 MPa (see (4.1)). The minimum volume is reached 115 ns later. Thereby, the bubble gas contents are highly compressed and a collapse shock wave is emitted (the shock wave with the smaller diameter in frame 4 of figure 7). While shock wave emission from the jet has been observed earlier with cylindrical shock collapsed bubbles (see e.g. Brunton 1970; Bourne & Field 1992, 1994, 1995), it was Ohl *et al*. (1995) who for the first time were able to unequivocally locate the origin of the two shock waves described above as the separate emission of a jet-induced and a bubble-collapse-induced shock wave in different pictures of a single photographic series by using the very high framing rate of 20 million frames per second. Two shock waves on *one* frame have been interpreted by Bourne & Field (1995) in the way confirmed here. Ward & Emmony (1991*b*) had observed the appearance of a jet shock wave and a collapse shock wave by using a single-shot Mach-Zehnder interferometer technique.

The earlier beginning of jet formation at smaller γ-values results in a greater time interval between the emission of jet shock waves and collapse shock waves. With $\gamma = 1.9$, the interval is 420 ns (figure 8*a*) with $\gamma = 1.7$, increases to 900 ns (figure 8*b*). In addition, the jet shock wave becomes weaker, as the velocity of the collapsing lower bubble wall is even lower if the jet impacts earlier (see figure 4, $\gamma = 1.6$: relative velocity between jet and bubble wall is about 127 m s^{-1}).

The following figures only show those collapse events which take place in contact with the solid boundary as only they have been found to cause damage. To obtain a three-dimensional impression of the collapsing bubble and the locations of the emission centres of shock waves, each figure shows a side-view and a bottom-view sequence of the collapse (see e.g. figures 9*a* and 9*b*). As they are taken from two

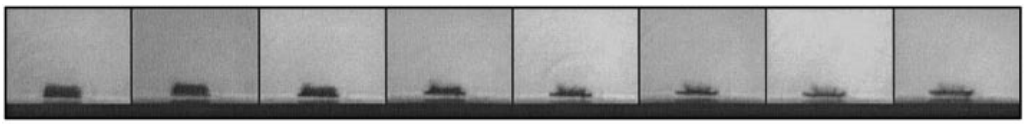

(*a*)

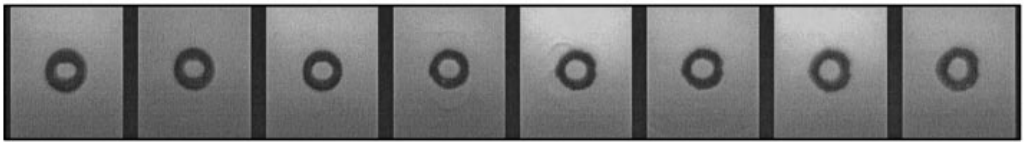

(*b*)

FIGURE 9. First collapse of a cavitation bubble in the neighbourhood of a solid boundary. $R_{max} = 1.45$ mm, $\gamma = 0.9$, 10^6 frames/s: (*a*) side view, frame width 4.0 mm; (*b*) bottom view, frame width 3.6 mm.

different bubbles (having identical parameters, of course), minor differences in bubble shape or shock wave emission may be present.

At the moment of the first collapse, the bubble touches the boundary when its initial distance is smaller than about $\gamma = 0.9$ (compare figures 2*f* and 2*g*). During collapse, the relatively broad jet flows through the bubble and radially outwards along the solid surface. Thus, the fluid flow directed to the bubble centre at the beginning of collapse becomes a ring vortex movement in the later stage of collapse. Therefore, the minimum bubble volume at this γ-value is relatively large and only weak shock waves are emitted (figures 9*a* and 9*b*, frame 5 of each). This visual observation agrees well with the acoustic measurements of Vogel & Lauterborn (1988), who found a strong decrease in sound emission for γ-values of about 0.9. The radial jet flow along the boundary has the second effect that the horizontal collapse movement of the bubble is retarded resulting in an increased diameter of the toroidal bubble at the moment of first collapse, when γ is decreased (compare figures 2*g* and 2*h*). This fact is important when comparing the damage patterns with bubble dynamics (see below).

At increasingly smaller γ-values, the strong elongation in an early stage of the collapse (e.g. in figure 2*h*, $\gamma = 0.6$, the bubble even has a nearly triangular shape) leads to increasingly larger jet diameters during first collapse. Thus, the inner diameter of the toroidal bubble becomes larger and larger, whereas the outer diameter remains nearly constant ($\gamma = 0.5$, figure 10*b*). Effectively, the bubble is collapsing from inside. Owing to the stabilizing vortex flow, the bubble volume is compressed symmetrically leading to a violent collapse, where the bubble torus disintegrates into many tiny bubbles along the ring, which collapse almost simultaneously, each emitting a shock wave (figure 10, frame 3).

At $\gamma = 0.3$, the torus collapses highly regularly such that its gaseous content is compressed without decay of the bubble. The emission of shock waves starts at those locations where the pressure is maximal (this is the case at the top and bottom in figure 11*b*, frame 4). The shock waves detaching from these regions move along the ring and further amplify the compression. At the meeting point on the ring, the pressure amplitude presumably is the highest. The assumption of orbiting shock waves is confirmed by the position of the centres of the waves in frame 5 of figure 11(*b*): they are located at the left- and right-hand side on the collapsed torus. The gliding collapse comes to an end by collision of the four moving collapse points.

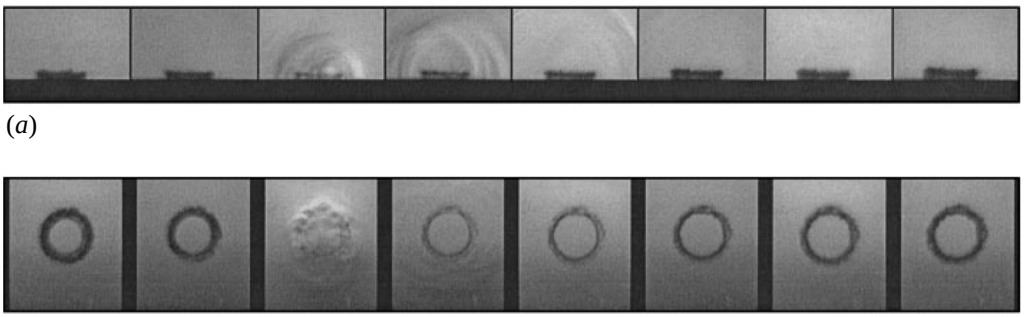

(*a*)

(*b*)

FIGURE 10. First collapse of a cavitation bubble; $\gamma = 0.5$. Other parameters are as figure 9.

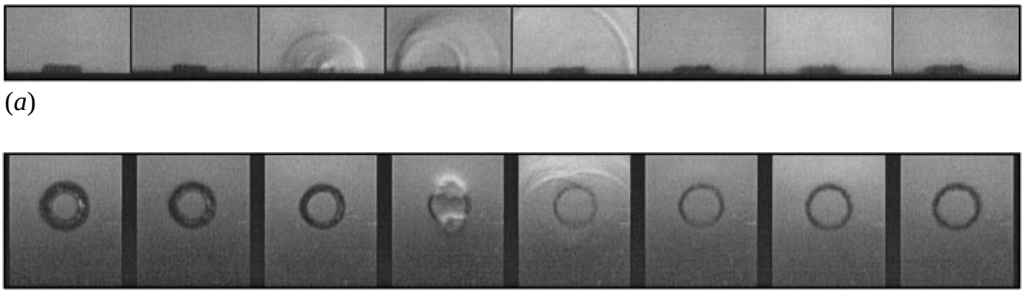

(*a*)

(*b*)

FIGURE 11. First collapse of a cavitation bubble; $\gamma = 0.3$. Other parameters are as figure 9.

The second collapse of a bubble proceeds in contact with the solid boundary for larger initial distances than the first collapse due to the cumulation of the accelerating forces during the first and second collapse phases. When γ is smaller than about 2, the bubble has reached the boundary at the moment of second collapse (see figure 2*b*,*c*) and therefore is capable of damaging the surface. At even larger initial distances (e.g. $\gamma = 3$, figure 2*a*), the formation of a vortex ring in the second collapse phase due to the jet flow is already visible, moving towards the solid boundary. But as only a small amount of water flows through the bubble as a thin jet, the radial collapse flow dominates in this γ-range. In the example where $\gamma = 3$, the distance of the collapsed bubble from the boundary is still greater than 3 mm after the second oscillation cycle and damage is impossible. This radial, centred collapse movement dominates down to about $\gamma = 1.8$. Figure 12(*a*), $\gamma = 1.9$, shows the subsequent emission of three shock waves from about the same centre just above the solid boundary. The bottom-view sequence (figure 12*b*) shows that only the separated small part above the main bubble (visible as a thin ring around the main bubble in frame 4 of figure 12*b*) collapses as a torus.

A bubble at $\gamma = 1.7$ shows the transition to a toroidal collapse (figure 13). The jet, being stronger for smaller γ-values, in conjunction with the smaller distance causes a more pronounced liquid flow along the boundary, accelerating the vortex flow around the bubble. This bubble torus collapses about 200 μm above the solid boundary (see figure 13*a*). Below the torus, right at the boundary, the rest of the bubble is visible, separated during collapse due to the highly curved upper bubble wall (see figure 2*c*,

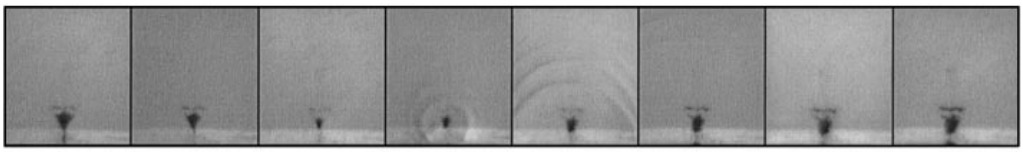

(*a*)

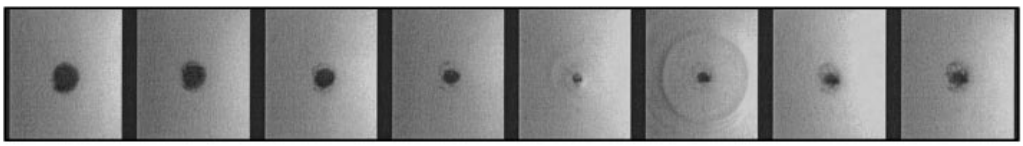

(*b*)

FIGURE 12. Second collapse of a cavitation bubble; $\gamma = 1.9$. Other parameters are as figure 9.

(*a*)

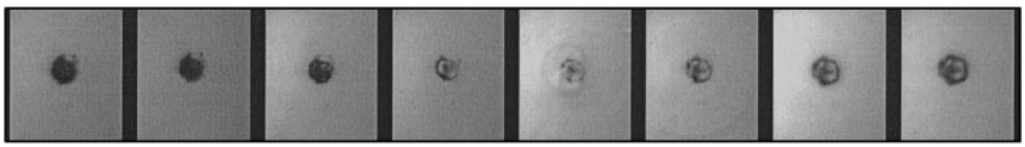

(*b*)

FIGURE 13. Second collapse of a cavitation bubble; $\gamma = 1.7$. Other parameters are as figure 9.

frame 14). Shock waves are emitted from the torus as well as from the bubble remains at the surface; about five different waves are discernible.

At a normalized distance of $\gamma = 1.4$, the jet flow through the bubble and radially along the boundary has increased in strength, leading to the formation of a pronounced vortex ring after the first collapse (see figures 2*e* and 14). The bubble torus collapses in direct contact with the solid boundary, decaying into several parts. In most of the cases, two shock waves are emitted at the rear and front end in the laser beam direction (figure 14*b*: left- and right-hand side) within a short time interval. The fact, that the axis of symmetry is parallel to the optical axis suggests that the form of the plasma generated (elongated cone) influences the torus behaviour. The small asymmetry at the bubble generation obviously transfers to the moment of second collapse, leading to a slow collapse at the upper and lower sides, as seen in figure 14(*b*). In some cases, up to five shock wave emission centres have been observed. The jet flow along the solid boundary additionally slows down the horizontal collapse movement. Consequently, the horizontal bubble diameter remains constant ($\gamma = 1.6$, figure 2*d*, frames 9 to 16) or even expands ($\gamma = 1.4$, figure 2*e*, frames 9 to 17). Thus, the diameter of the collapsed torus increases with decreasing γ: figure 14, with $\gamma = 1.4$, shows diameters of 1.95 mm (*a*) and 1.8 mm (*b*) in contrast to only about 0.8 mm at $\gamma = 1.7$ (figure 13*b*).

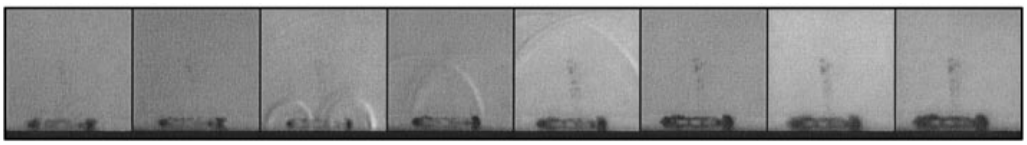

(*a*)

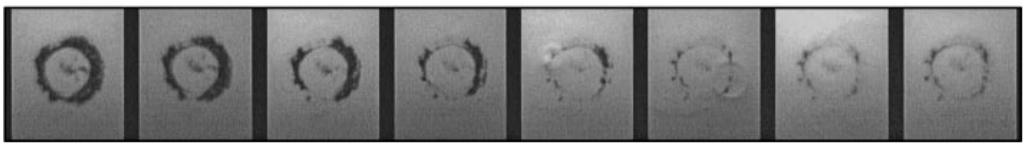

(*b*)

FIGURE 14. Second collapse of a cavitation bubble; $\gamma = 1.4$. Other parameters are as figure 9.

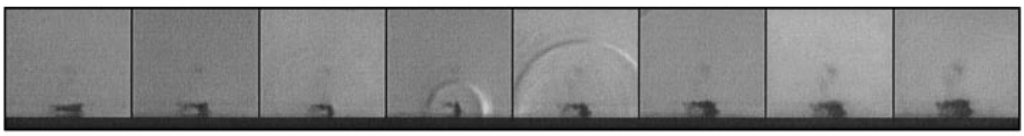

(*a*)

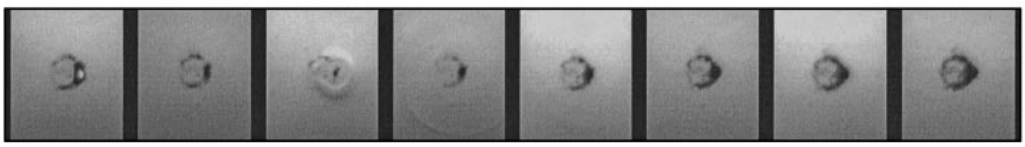

(*b*)

FIGURE 15. Second collapse of a cavitation bubble; $\gamma = 1.2$. Other parameters are as figure 9.

If γ is reduced to 1.2, the horizontal expansion by the jet flow coincides with the bubble expansion phase, as the jet hits the boundary earlier (see figure 2*f*). The following collapse movement is scarcely slowed down and consequently the size of the torus becomes smaller again (figure 15*b*, diameter of the torus is 820 μm). As the torus is thinner at the left-hand side in figure 15(*b*), the collapse starts there and again goes around the torus. When the gliding collapsing parts (from the top and bottom sides of the torus in figure 15*b*) meet each other at the laser-facing side, a strong shock wave is emitted from this point (right-hand side in figure 15*b*). In some cases, weak shock waves are emitted from the opposite side on the torus bubble as well.

Now, if γ is reduced further and thus the jet appears even earlier, there is a certain initial distance to the boundary (or a certain γ) from which distance (or γ) the jet slows down the horizontal movement of the bubble during the first collapse (see figure 2*g*, $\gamma = 0.9$), leading to an increased diameter of the vortex ring generated. By this effect, the diameter of the torus at the second collapse is increased, too, compared to the torus size at $\gamma = 1.2$ (see figures 15 and 16). Figure 16(*b*) shows that at $\gamma = 0.9$ the torus decays into two separate parts at the left- and right-hand sides when viewed in the beam direction. As the left part collapses to a smaller volume than the right part, the emitted shock wave is stronger (to be seen at the bottom of figure 16*b*). The effect of the second collapse on the surface becomes weaker from about $\gamma \leqslant 1$, as the radial collapse flow has already been converted to a vortex ring flow during the first collapse phase.

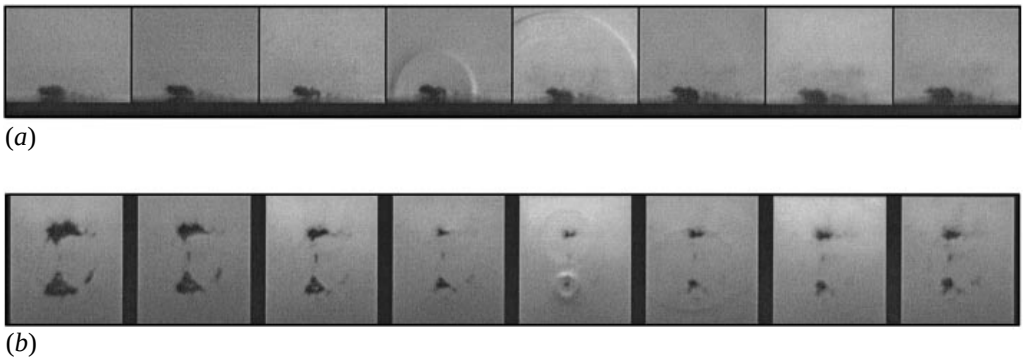

(*a*)

(*b*)

FIGURE 16. Second collapse of a cavitation bubble; $\gamma = 0.9$. Other parameters are as figure 9.

The third collapse is not expected to cause distinct damage mainly for two reasons. On the one hand, the transformation from a mainly radial first collapse to a torus-shaped second one (in the range of $\gamma \geqslant 1$) leads to a further, weaker torus collapse. Forced by the jet flow, the bubble volume expands as a torus at the boundary surface (compare e.g. figures 2*c* and 2*e*). At the moment of the third collapse, the torus decays into many individual bubbles, as frame 22 of figure 2(*e*) shows. Thus, the overall energy of the torus bubble is divided between the tiny bubbles and the compression pressure of a single bubble is smaller. However, a large part of the maximum potential energy of the bubble has been dissipated by viscous fluid flow and the emission of shock waves during the first and second collapse (Vogel & Lauterborn 1988). Consequently, less energy is available at the moment of third collapse and damage is unlikely; only at $\gamma = 2.0$ does the nearly radial third collapse have to be considered (figure 2*b*, frame 21).

There is an interesting deviation from the translation towards the solid boundary. In a small range from about $\gamma = 1.0$ to 1.2, the centre of the bubble first translates towards the boundary, but after the second collapse, it moves away again ('Ping-Pong' movement, see figure 2*f*). Similarly to the argument for different torus diameters at the second collapse, this effect is caused by the time-delayed collapse of the side walls of the bubble compared to that of the bubble top wall. With reduced initial distance, jet formation and thus the radial flow onto the boundary starts earlier, causing a mainly horizontal expansion of the bubble after the first collapse. At the moment which is denoted as second collapse (figure 2*f*, frame 17), the vertical collapse is finished first due to the smaller expansion. Nevertheless, the horizontal collapse movement continues, further increasing the inner pressure of the bubble (frame 18). Therefore, the upper bubble wall expands again while the horizontal bubble diameter remains nearly constant and consequently the centre of the bubble rises. At the moment of third collapse, the distance of the bubble to the boundary is about 1 mm.

3.2. *Erosion patterns*

3.2.1. *Variation of bubble distance*

Figure 17 gives an overview of the resulting damage on a soft material (aluminium) in the range $\gamma = 2.2$ to 0.3. Each specimen was exposed to 100 identical bubbles, which were generated sequentially above the centre of the area shown. This technique gives information on even very weak bubble-caused forces using the superposition of 100 single effects. The pictures were taken using an optical microscope with differential interference contrast in order to obtain visible contrast even with small

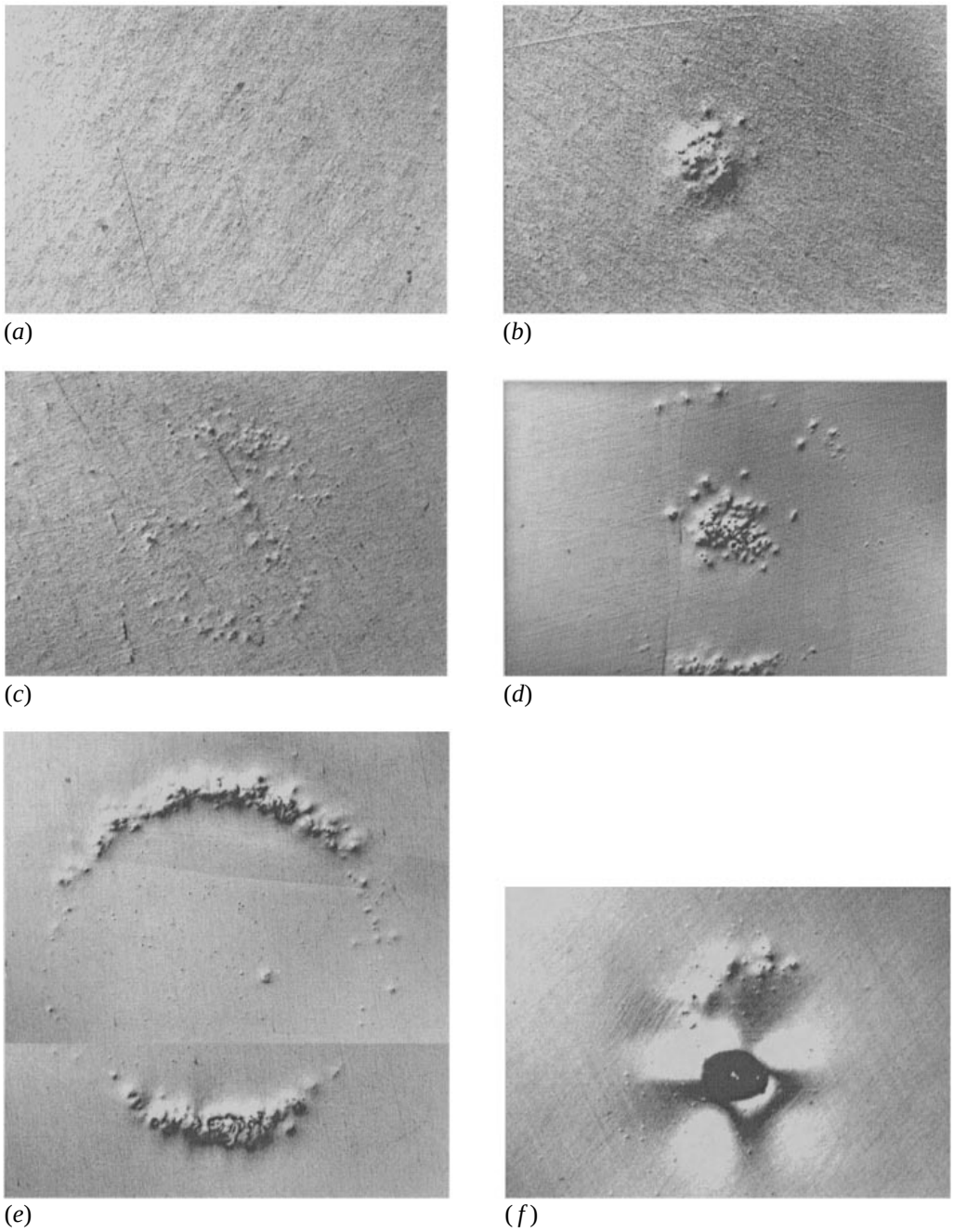

FIGURE 17 (*a–f*). For caption see facing page.

height differences. The direction of the laser beam goes from the bottom to the top in each picture. The maximum bubble radius was held constant for all specimens in the series ($R_{max} = 1.45 \pm 0.03$ mm).

At $\gamma = 2.21$ (figure 17*a*) or above, there was no visible damage. In the range of $\gamma \leqslant 2$, damage was always found after the generation of 100 bubbles. The structure

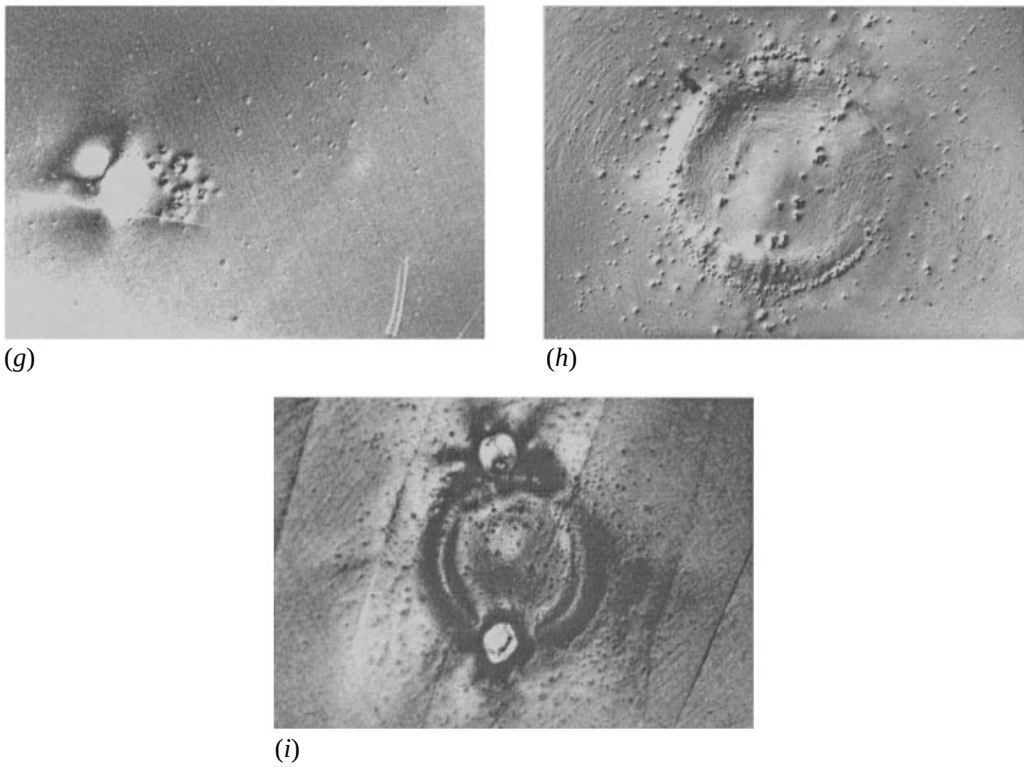

FIGURE 17. Damage on aluminium specimens caused by 100 cavitation bubbles. $R_{max} = 1.45$ mm, frame width 2.6 mm: (*a*) $\gamma = 2.21$; (*b*) $\gamma = 1.91$; (*c*) $\gamma = 1.69$; (*d*) $\gamma = 1.52$; (*e*) $\gamma = 1.41$; (*f*) $\gamma = 1.21$; (*g*) $\gamma = 0.90$; (*h*) $\gamma = 0.69$; (*i*) $\gamma = 0.31$.

of the damage pattern changes distinctly as the initial distance is varied. For example at $\gamma = 1.91$, figure 17(*b*) shows a relatively concentrated field of single indentations in a region of size 480 μm. Figure 18(*a*), obtained with the Micromap interference microscope, gives a three-dimensional impression of the same region. The depth of the indentation is coded in grey scales (colour-coded in the original) for better visualization. The maximum depth was about 7 μm.

When γ is reduced, the size of the damaged region increases (figures 17*c* to 17*e*). The damage pattern at $\gamma = 1.69$ can be viewed as a ring plus central damage, not fully separated yet. At $\gamma = 1.41$, all pits are located on a ring with a diameter of 1.9 mm (figure 17*e*). Figure 18(*b*) shows a section of the rear part of the ring (in the laser beam direction) in detail.

The damage pattern after the collapse of 100 identical bubbles gives information about the geometry of the damage distribution relative to the bubble position (i.e. central or circular pattern) as well as about the variation of impact locations from bubble to bubble. If only one single bubble is generated above a particular position, the number of indentations caused by that bubble's dynamics is obtainable. For example, when γ is about 1.4, at least two pits are produced, which are located diametrically on a (virtual) circle. Figure 19(*a*) ($\gamma = 1.41$) shows these two pronounced pits and, additionally in this case, four weaker indentations. The Micromap analysis reveals a maximum depth of the two strongest pits (bottom and top in figure 19*a*) of 3 and 1.2 μm, respectively.

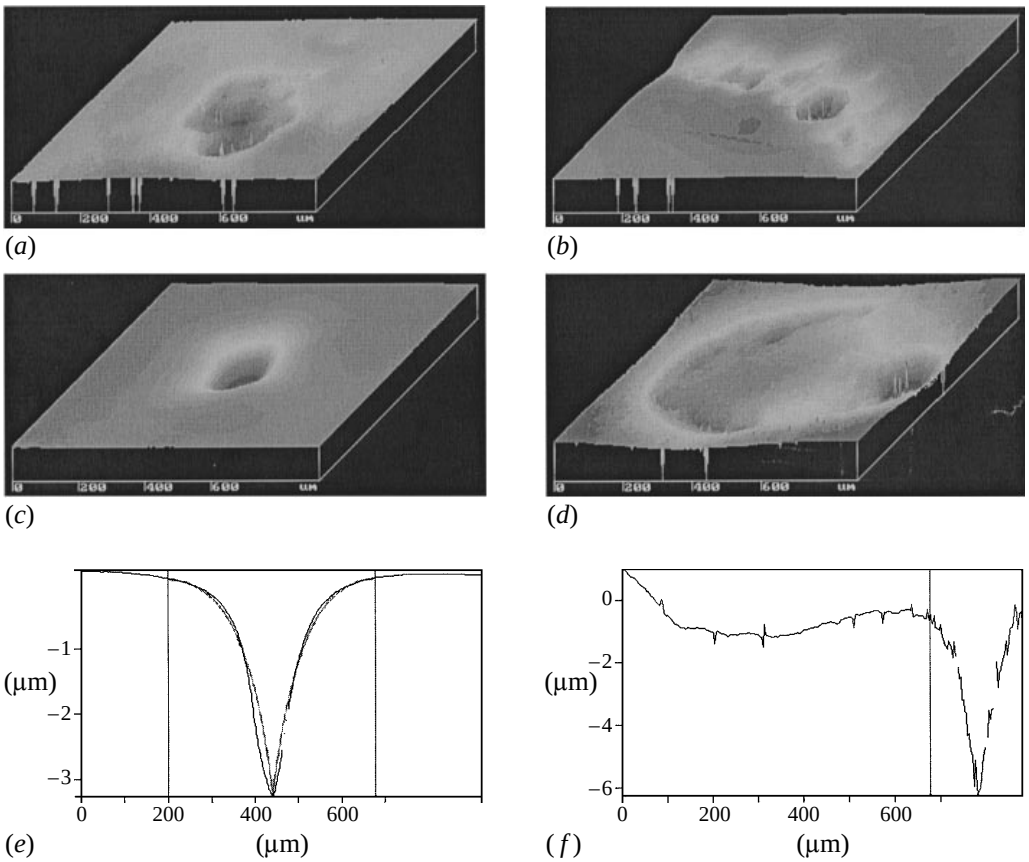

FIGURE 18. Microscopic view of the damaged area taken with the phase-shifting interference microscope; the depth is grey-scale coded, $R_{max} = 1.45$ mm: (*a*) $\gamma = 1.91$, 100 bubbles, maximum depth 7 μm; (*b*) $\gamma = 1.41$, 100 bubbles, part of the damage ring; (*c*) $\gamma = 1.21$, 1 bubble, maximum depth 3.4 μm; (*d*) $\gamma = 0.31$, 1 bubble, maximum depth 7.1 μm; (*e*) surface profile of the pit in (*c*), the inner curve is a quadratic exponential fit of the measured data (see text); (*f*) surface profile of the pit in (*d*).

If γ is further reduced, the circle on which the pits are located becomes smaller at first (figures 17*f*, $\gamma = 1.21$), but then larger again (figures 17*g* to 17*i*, $\gamma = 0.90$ to 0.31). Moreover, the distribution around the circle changes: while at $\gamma = 1.41$ the pit distribution at the laser-facing and opposite parts of the circle is nearly the same and at both sides fewer pits are visible, nearly all pits accumulate at a point in the lower part of the circle for $\gamma = 1.21$. The remaining part of the ring shows only a few indentations. However, the existence of these pits supports the view that the deep indentation is located on a circle and not centrally below the bubble. After the collapse of only one bubble, a single pit is visible (figure 19*b*), which allows no localization relative to the bubble. The Micromap analysis (figure 18*c*,*e*), gives the depth (3.4 μm) and diameter (479 μm) of this pit. The characteristic damage pattern at $\gamma = 0.9$ (figure 17*g*) shows on the left-hand side a big indentation with small pits on its right-hand side. Additionally, detailed inspection reveals a very weak deformation at the right hand side of figure 17(*g*), about 1.4 mm from the deep one. Thus, again two pits are located on a circumference.

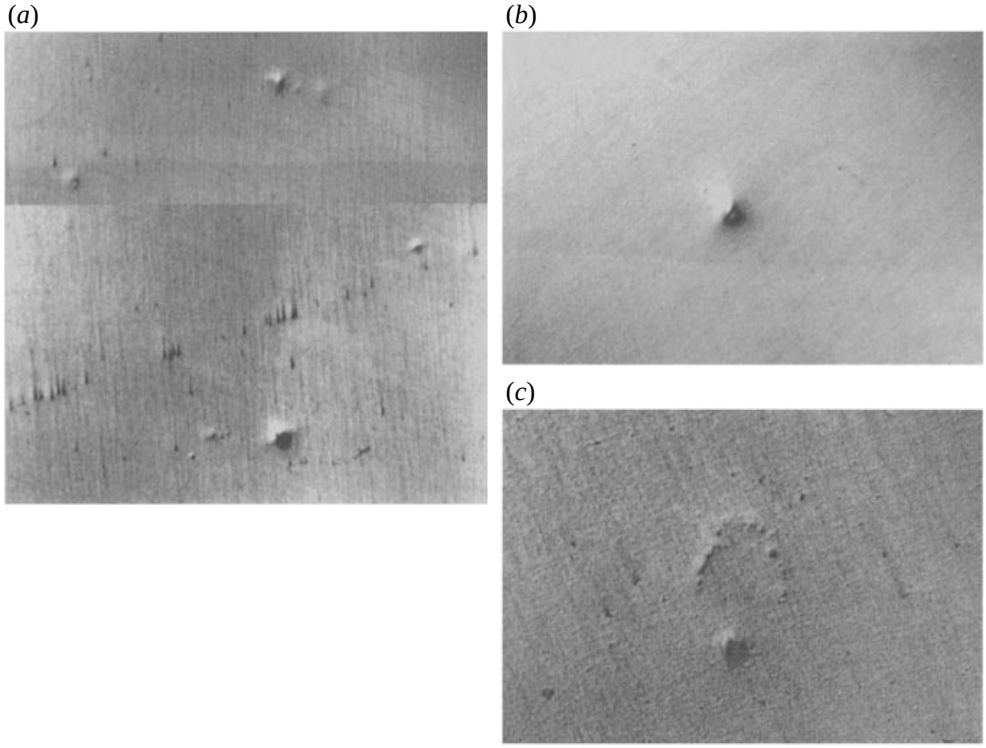

FIGURE 19. Damage on an aluminium specimen caused by one single cavitation bubble; $R_{max} = 1.45$ mm: frame width 2.6 mm: (*a*) $\gamma = 1.41$, (*b*) $\gamma = 1.21$, (*c*) $\gamma = 0.31$.

A more regular pattern can be found at very small initial distances. The overall damage at $\gamma = 0.69$ consists of three different components (figure 17*h*): first a circle composed of many tiny pits, secondly a smooth indentation of the whole interior of this circle and third a superposition over the whole region of statistical distributed smaller and larger pits. At the smallest initial distance presented here, very pronounced damage is visible after the influence of 100 identical bubbles (figure 17*i*, $\gamma = 0.31$). The circle is slightly oval (diameter parallel to the laser beam 1.0 mm, perpendicular to it 0.84 mm) with two deep pits at the front and rear sides. Even one single bubble produces several pits along an oval, where the deepest is located at the laser-facing side (figure 19*c*). The profile line through this damaged region shows a maximum depth of 7.1 μm and a shallow indentation inside the oval (figure 18*d,f*).

The quantitative analysis of the damage produced by one single cavitation bubble in the range $\gamma = 0.3$ to 3.0 is displayed in figures 20 and 21. Figure 20 shows the maximum depth of the pits which are found after the generation of only one bubble at a given distance from a specimen surface made of pure aluminium. There are relatively large variations from bubble to bubble at the same γ-value. However, a clear result from these measurements is that damage starts only at normalized distances of less than $\gamma = 2$. The strongest indentations are observable in the range $\gamma = 1.2$ to 1.4 and about $\gamma \leqslant 0.3$; the maximum depth of 8.4 μm is reached at $\gamma = 0.31$. Of course, the influence of 100 bubbles at the same position of a specimen produces much larger indentations: at $\gamma = 0.3$, a depth of 130 μm was measured.

The diameter of the individual pits was measured 50 nm below the specimen surface in order to get a well-defined value, and at fixed bubble parameters shows variations

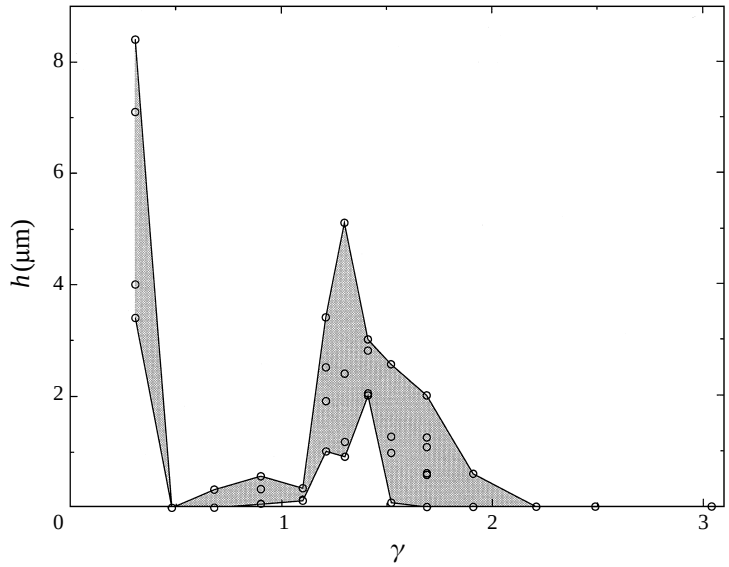

FIGURE 20. Maximum depth of the damage produced by one single cavitation bubble on an aluminium specimen, $R_{max} = 1.45$ mm.

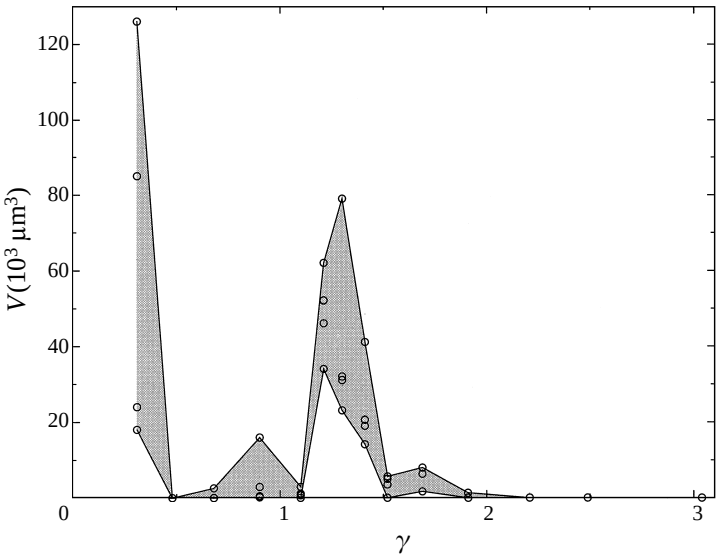

FIGURE 21. Volume of the deformation produced by one cavitation bubble on aluminium.

as well. The widest pits are produced by bubbles at $\gamma = 1.2$: the maximum diameter is 570 μm. Moreover, at this γ-value the variation is the smallest, i.e. the erosion mechanism is the most stable one.

In order to estimate the volume of an indentation, the profile was fitted by a quadratic exponential function, whose parameters are the pit depth h and the radius r at 50 nm depth. This fit is shown in figure 18(*e*) as the inner curve. Other mathematical approximations of the measured profile, e.g. by parts of a sphere or a cone, lead to greater average errors. Figure 21 shows the dependence of pit volume, from one

γ	Figure	Damage pattern by 100 bubbles	Size of damaged area
$\geqslant 2.2$	17(*a*)	no damage	—
1.9	17(*b*)	concentrated field of pits	480 μm
1.7	17(*c*)	ring with centred pits (not yet fully resolved)	960 × 1360 μm^2
1.5	17(*d*)	ring with centred pits	1800 μm
1.4	17(*e*)	ring	1900 μm
1.2	17(*f*)	ring	700 μm
0.9	17(*g*)	two indentations on a ring	1400 μm
0.7	17(*h*)	ring and smooth indentation	1100 × 1300 μm^2
0.3	17(*i*)	oval ring and smooth indentation	840 × 1000 μm^2

TABLE 1. Variation of damage patterns with γ; $R_{max} = 1.45$ mm.

single cavitation bubble, on the distance γ. The plotted volume was obtained by summing the individual volumes of all pits which were generated by the bubble. The observable deviations at a fixed γ-value are partly caused by the assumption of rotational symmetry of the pits, which is not valid in all cases. Nevertheless, the variation of erosion properties of a cavitation bubble with initial distance from the specimen surface are quite obvious. The extremely complicated dependence of the damage pattern on the normalized distance γ is summarized in table 1.

3.2.2. *Variation of bubble size and number*

The characteristics of bubble dynamics are only dependent on the normalized distance γ, and not explicitly on the maximum radius R_{max} at least for a certain range of bubble sizes. For example, at $\gamma = 1.4$ the bubble at its second collapse will be toroidal, independent of the maximum size of the bubble. The size only determines the diameter of the torus. Therefore, it can be expected that at constant γ the damage pattern is the same for all bubble sizes. Hence, the amount of damage (i.e. the volume of the pits) and the diameter of the damaged region should scale with R_{max}. These assumptions are proved by figure 22, showing the damage to aluminium by 100 bubbles in the range of $R_{max} = 1.0$ mm to 3.0 mm at $\gamma = 1.4$. The damage pattern is largely the same for all bubble sizes: the individual pits generated by each of the 100 bubbles accumulate on a circle. Owing to the poorer quality of the material of the specimen (at $R_{max} = 1$, 2 and 3 mm), the surface shows additional pits, which cover the specimen homogeneously (see figure 22*a*) and were present before the experiments. The damage ring resulting from bubbles with $R_{max} = 3.0$ mm is not clearly limited as in the case of the smaller bubbles. Probably this is caused by the influence of the environment of the bubble (walls of the cuvette, edge of the specimen), which becomes more important for the dynamics of larger bubbles. The diameter of the damage circles (1.3, 1.9, 2.6 and 3.1 mm) is directly proportional to the size of the bubbles: it is 1.25 times the maximum bubble radius. Only the largest radius shows a deviation of 0.6 mm from this proportionality, probably also caused by the perturbation due to the cuvette walls.

The development of the erosion process with repeated impact of identical cavitation bubbles on an aluminium specimen is shown in figure 23 ($\gamma = 1.41$, $R_{max} = 1.45$ mm). Six different positions on the surface are exposed to the dynamics of 1, 5, 10, 20, 100 and 5000 bubbles, respectively. As shown before, at this γ-value several pits are generated by one bubble, which appear on the circumference of a circle. Therefore, the successive influence of multiple bubbles results in an accumulation of these

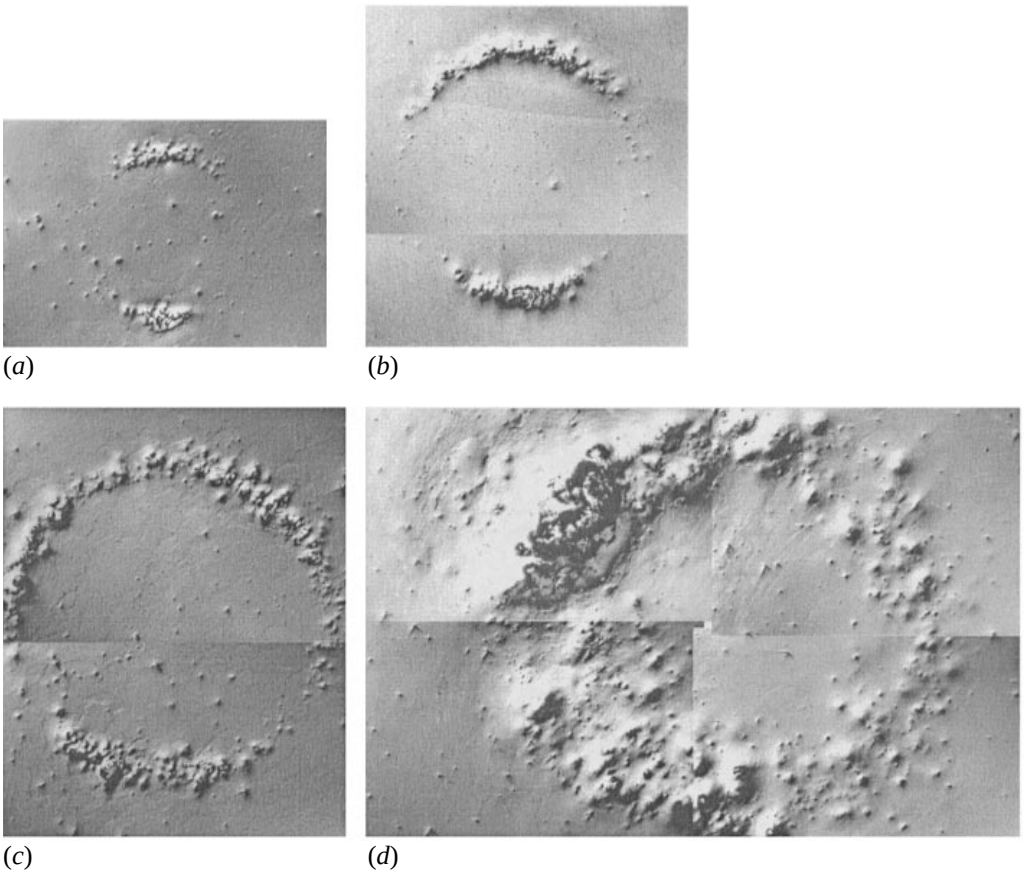

FIGURE 22. Damage on aluminium generated by 100 bubbles for four different maximum bubble sizes, $\gamma = 1.4$: (*a*) $R_{max} = 1.0$ mm, frame width 2.6 mm; (*b*) $R_{max} = 1.45$ mm, frame width 2.6 mm; (*c*) $R_{max} = 2.0$ mm, frame width 2.8 mm; (*d*) $R_{max} = 3.0$ mm, frame width 5.2 mm.

indentations along the circumference (see figure 23*a–d*). After a great number of bubbles, the probability of generating an impact at a location already damaged becomes greater, leading to an increased deformation around the circle. After 5000 bubbles, the specimen shows severe damage. Especially at the surface facing the laser (lower side in figure 23), deep craters with sharp edges are generated. This may be an indication of the beginning of material loss. Remarkably, neither the centre of the circle is damaged even after 5000 bubbles nor have the main locations of the pits (in the front and rear part of the circle) changed. Thus, it can be concluded that even an irregular surface with severe deformations as accumulated here in the course of damage has no substantial effect on the bubble dynamics.

3.2.3. *Erosion of various materials*

In order to analyse the dependence of cavitation damage on the surface hardness, three more materials are investigated (all material data from Domke 1987): brass (Ms 58, Brinell hardness HB 85, yield strength $R_{p0.2} = 170$ MPa), mild steel (St37–2, Vickers hardness HV 110, $R_{p0.2} = 235$ MPa) and ferrite austenic duplex steel (G–X 4 CrNiMoN 27 5 2, HV 245, $R_{p0.2} = 483$ MPa). $R_{p0.2}$ describes the pressure that causes a deformation of 0.2% of the overall thickness of the test specimen after taking off the

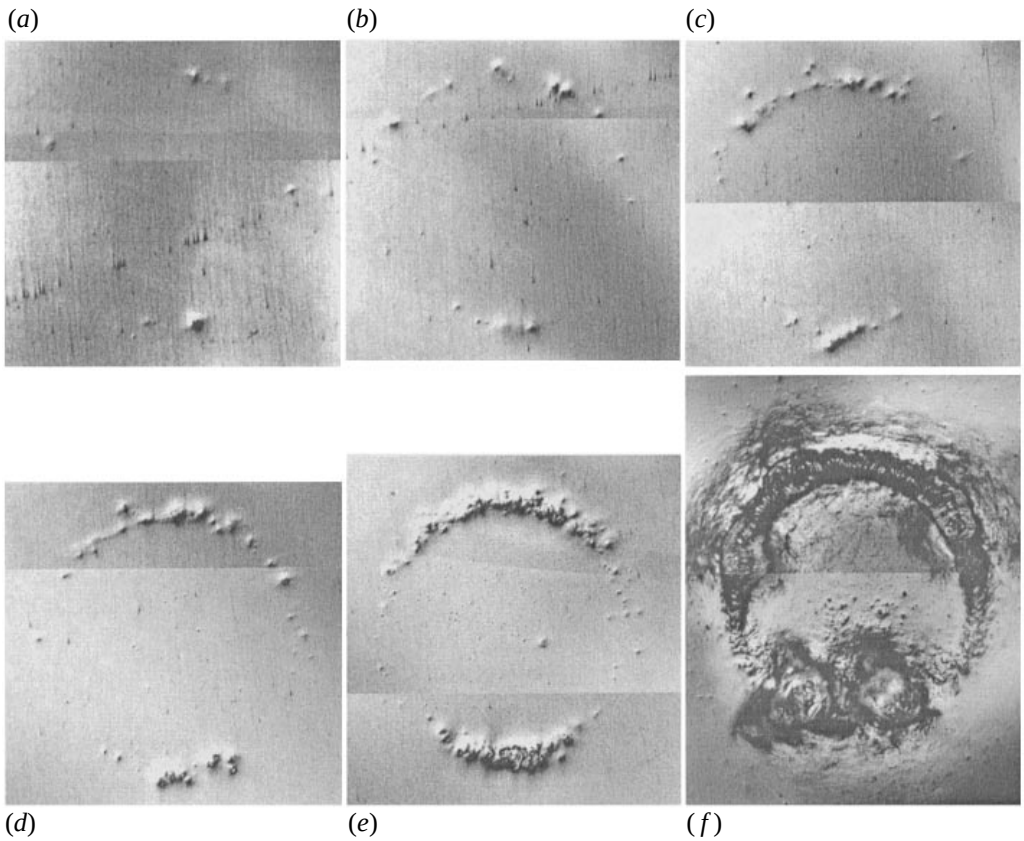

FIGURE 23. Development of the erosion process with increasing number of cavitation bubbles applied (on six different specimens); $R_{max} = 1.45$ mm, $\gamma = 1.41$. Number of bubbles applied: (*a*) 1, (*b*) 5, (*c*) 10, (*d*) 20, (*e*) 100, (*f*) 5000; frame width 2.6 mm.

load. The Brinell hardness of pure aluminium, as used in the experiments described before, is about 15, its yield strength is 16 MPa. The specimens are exposed to 1, 100 or 5000 cavitation bubbles with a maximum radius of 1.45 mm. The distance to the boundary was chosen in a way that was varied, and large damage could be expected. The average value was $\gamma = 1.28 \pm 0.03$ for all specimens.

Figure 24 shows the damaged regions of the three materials. As single bubbles cause no detectable damage, only those for 100 bubbles (left-hand column) and 5000 bubbles (right-hand column) are shown. A comparison with the deep indentations produced on aluminium by 100 bubbles (figure 17*f*) immediately reveals that the amount of damage is strongly dependent on the yield strength of a material. Even with brass, whose yield strength is greater by only a factor of six, the plastic deformation is much smaller than with aluminium. Quantitative measurements with the Micromap interference microscope confirm this statement: whereas on soft aluminium the maximum depth after impingement of 100 bubbles was 43 μm, it was 1.27 μm on brass, 0.41 μm on mild steel and as small as 0.1 μm on duplex steel. Thus, the greater yield strength of mild steel, increased by a factor of 15 compared to aluminium, results in an indented depth which is smaller by a factor of 100.

Of course, the erosion pattern is independent of the material used. Accordingly, on the brass specimen the formation of a circle with a strong concentration of the

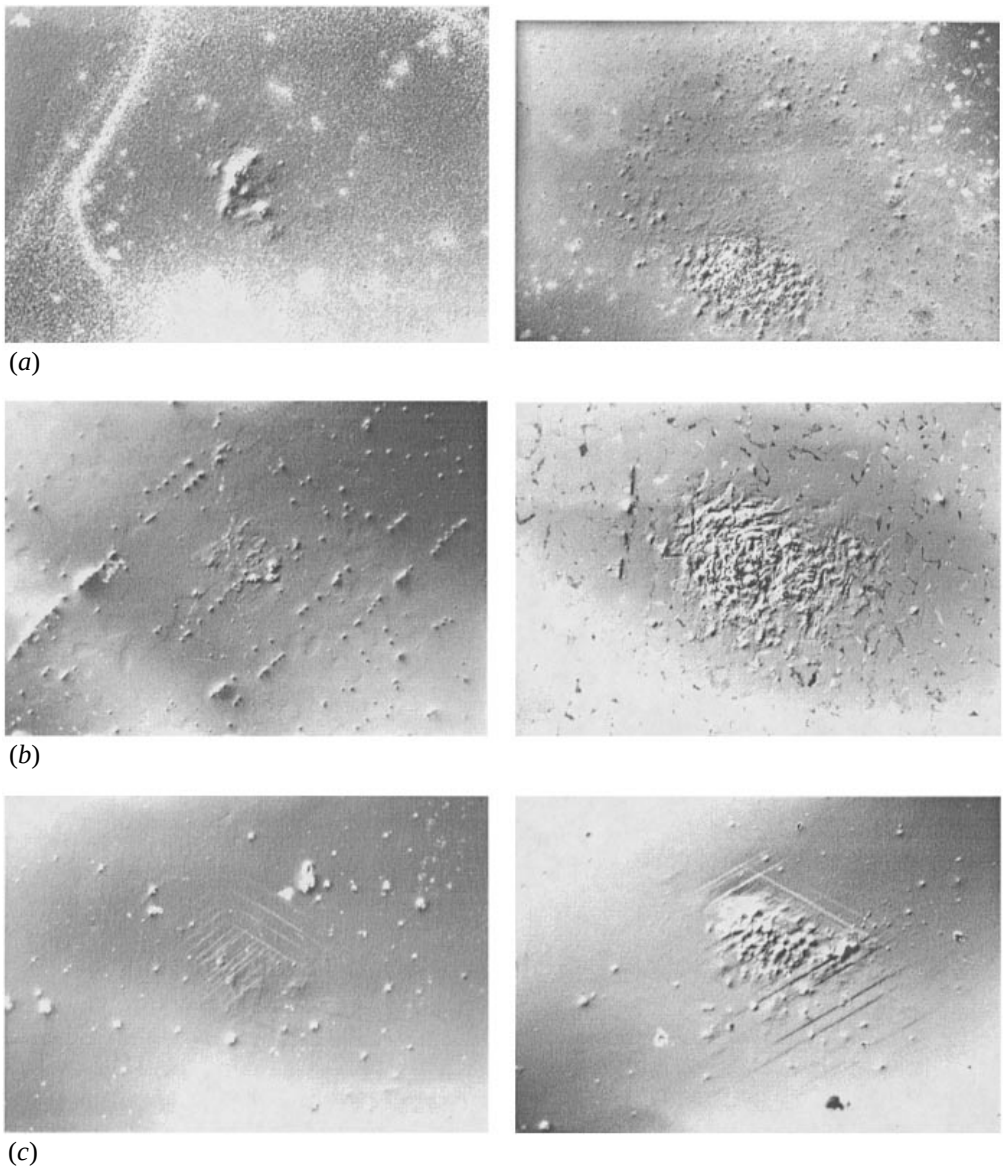

FIGURE 24. Erosion of various materials by cavitation bubbles; $R_{max} = 1.45$ mm, $\gamma = 1.28$; left-hand column: 100 bubbles, right-hand column: 5000 bubbles; frame width 1.3 mm (execpt (*a*), right frame: width 2.6 mm): (*a*) brass; (*b*) mild steel; (*c*) duplex steel.

individual pits in the front region is visible, as expected for this initial distance (figure 24*a*, right picture). On the harder materials, the relatively few pits in the rear part of the circle are not visible. Compared to aluminium, the concentration of pits at the laser-facing side does not produce a single, deep indentation but a damage field composed of multiple pits. This difference presumably can be explained by the difference in the yield strength, too. Caused by the smaller plasticity of harder materials, not only the depth but also the diameter of an indentation becomes smaller (according to the measurement process of the Brinell hardness with a sphere as indentation object). On aluminium, every cavitation bubble produces a 500 μm sized

indentation on average. As the lateral variation of the damage location is small at this γ-value, the overlap of each of the pits is substantial. Thus, the indentation becomes deeper with every bubble, but hardly wider. With harder materials, the lateral variation is as small as before (about ± 80 μm at 100 cavitation bubbles on brass, see figure 24*a*, left picture), but as the diameters of the individual pits are very small, as the material is much more resistive against deformation, the overlap is small and a field of homogeneously scattered pits is produced.

4. Discussion

4.1. *Damage capability of the jet*

The impact of a liquid jet on a (solid) surface generates a water hammer pressure (Cook 1928; de Haller 1933). This pressure is linearly dependent on the jet velocity (acoustic approximation; when treating the problem as a nonlinear one, the water hammer pressure at impact velocities less than 200 m s^{-1} is only marginally greater (Lush 1983)):

$$p_{\mathrm{wh}} = \frac{\varrho_w c_w \varrho_{\mathrm{sb}} c_{\mathrm{sb}}}{\varrho_w c_w + \varrho_{\mathrm{sb}} c_{\mathrm{sb}}} v_{\mathrm{imp}} \tag{4.1}$$

where ϱ_w and c_w are the density and sound velocity of the jet medium, respectively, and ϱ_{sb} and c_{sb} are the corresponding values for the solid boundary. Assuming aluminium as the specimen material, the resulting water hammer pressure for $\gamma \geqslant 1.2$ ($v_{\mathrm{imp}} \leqslant 25$ m s^{-1}, see figure 6) is as low as 34 MPa. At $\gamma \leqslant 1$ the impact velocity rises to 83 m s^{-1}, corresponding to a water hammer pressure of about 110 MPa. When γ is very small ($\gamma \leqslant 0.2$), the liquid above the upper bubble wall impacts with a speed of 151 m s^{-1} onto the boundary and thus produces a pressure of about 200 MPa. In order to evaluate the possibility of plastic deformation by those water hammer pressures, they may be compared with the value of the yield strength $R_{p0.2}$ (Hornbogen 1983). The yield strength of pure aluminium (99.999%) is 16 MPa, for example. This comparison is not absolutely exact, as $R_{p0.2}$ is measured with a static load; the dynamical value is assumed to be higher.

When a dynamical load acts on a solid body, not only the applied pressure (for example the water hammer pressure of the jet) determines the resulting deformation, but also the duration of interaction. The shorter this duration, the smaller is the indentation, as this does not grow instantaneously. The duration of interaction is determined by the time the rarefaction wave (starting at the moment of impact from the border of the jet) needs to expand to the jet centre. Assuming a jet diameter of about 300 μm, the water hammer pressure acts for a time $\tau_w = R_{\mathrm{jet}}/c_0 \approx 0.1$ μs (R_{jet} is the radius of the jet, c_0 the sound velocity of water). After this, the pressure decreases to the stagnation pressure.

The possibility of jet-induced damage can be proved with the help of the erosion patterns. For example, in the range of $\gamma = 1.2$ to 1.9, pronounced surface deformation was observed (figures 17*b* to 17*f*), although the impact velocity and with it the deforming pressure was very small ($v_{\mathrm{imp}} \leqslant 25$ m s^{-1}). Moreover, the damage pattern at $\gamma = 1.4$ is circular; at the centre, where the jet impacts and the water hammer pressure has its maximum, no pits were found (figure 17*e*). Hence, a jet having this impact velocity (or, of course, a lower one) does not generate an indentation on the specimen. Thus it can be concluded that the damage patterns observed at $\gamma > 1$ on the aluminium specimen are definitely not caused by jet impact. This result can be explained by the relatively low pressure generated by the jet impact (when compared

with the bubble collapse pressure, see below) and, additionally, by the very short duration of the interaction.

When the initial distance to the boundary is reduced, the impact velocity (and the water hammer pressure, respectively) increases (see figure 6). Additionally, the interaction time becomes longer due to the greater jet diameter. As a jet-caused damage should be about rotationally symmetric and located at the centre, only a part of the damage found in the range $\gamma = 0.3$ to 0.7 (see figure 17*h,i*) could be generated by a jet, i.e. the smooth indentation covering the whole damaged area, mentioned in § 3.2.1. The pits around the oval ring and the statistically distributed pits are not explainable by a central impacting jet.

In a cloud of bubbles, a greater damage capability of the jets is possible. For example, the bubbles could be elongated perpendicular to the boundary by the influence of a flow field. Calculations by Voinov & Voinov (1976) have demonstrated that even small elliptical deformations of a bubble in this direction result in a doubling of the jet velocity. A second accelerating effect on the jet velocity may be the interaction of a shock wave, emitted by bubbles collapsing in the neighbourhood, with the jetting bubble (Dear, Field & Walton 1988; Philipp *et al*. 1993; Field 1994). Nevertheless, a recent work of Jungnickel (1995), who investigated the dynamics of two bubbles oscillating a small distance apart one above the other over a solid boundary either in or out of phase, reveals no increased jet velocity compared to a single bubble near a boundary. In most of the cases, she observed a smaller jet velocity due to a reduction of the elongation of the bubble prior to the jet formation.

4.2. *Erosion due to the collapse of a bubble at a solid boundary*

As the jet causes only a minor part of the damage observed in the range $\gamma = 0$ to 2, a different erosion mechanism exists. Shutler & Mesler (1965) concluded, by a comparison of damage patterns with the shape of the bubble, that the pressure at minimum bubble volume could be the cause of the erosion. This assumption is confirmed in the whole γ-range by the results presented here. The mechanism of cavitation erosion has its origin in the pressures generated by a bubble collapsing in direct contact with the solid boundary. This is the case at the first collapse with $\gamma \leqslant 0.9$ and at the second collapse with $\gamma \leqslant 1.9$.

A comparison of the bubble shape at the moment of collapse and the locations of shock wave emission with the damage pattern produced by 100 bubbles demonstrates how the deformation structures can be explained despite their great differences with varying γ. To this end, figure 25 shows those bubble collapses which are considered to cause damage (three pictures each of the bottom view sequences of figures 10 to 16 and the microscope pictures of the region damaged by 100 bubbles (depicted from figure 17) using equal scaling and orientation).

At about $\gamma = 1.9$, the second collapse of a bubble takes place in contact with the solid boundary. Thereby, the bubble collapses down to a single centre, emitting a shock wave (figure 25*a*, left-hand side). This pressure wave, i.e. the pressure inside the bubble when in contact with the solid boundary, causes an indentation on the surface. After the impact of 100 equal-sized cavitation bubbles, the pits accumulate inside a region of diameter 480 μm.

With decreasing γ, the bubble shape at the moment of second collapse changes to a torus. Shock waves are emitted by the collapsing torus (visible e.g. in the bottom-view frames of figure 25*b*, where γ was 1.7). Sometimes, the remaining bubble volume at the centre (which is nearer to the boundary at this γ-values than the torus) collapses violently, too, and emits a strong pressure wave, as shown with a different bubble

in figure 26 (side view). The size of the damaged region is increased (960 μm × 1360 μm), as shock waves are no longer emitted by only one centre but from the area covered by the torus. The torus diameter in figure 25(*b*) is even smaller (about 800 μm), but the diameter of the bubble shown in the side-view picture (figure 17) reaches 1260 μm. This difference is explainable by the strong γ-dependence of the bubble diameter at the moment of second collapse: while at $\gamma = 1.9$ the bubble collapses down to a point, at $\gamma = 1.4$ the torus is of size 1.9 mm. Thus, the variation of the distance to the solid boundary from bubble to bubble has a great effect on the torus diameter.

At $\gamma = 1.4$, the bubble collapses at the solid boundary in the form of a torus with a diameter of about 1.9 mm (figure 25*c*). Each bubble produces at least two pits, located on a circle according to the shock centres. After the generation of 100 bubbles, these pits have formed a circle, which is more pronounced at the front and rear sides presumably due to the asymmetry of the laser plasma.

The same agreement between geometrical shape of the bubble collapse and resulting damage as at $\gamma = 1.4$ is found at $\gamma = 1.2$ (figure 25*d*). As the horizontal collapse movement is no longer slowed down at this initial distance, the torus is smaller (diameter 820 μm), and with it the size of the damaged region (700 μm). Owing to the asymmetric thickness of the bubble torus, it collapses down to one single centre in the front region (lower part of the figure); accordingly, the main part of the damage consists of a deep crater at that location.

From $\gamma \leqslant 0.9$, the bubble already touches the boundary at the moment of first collapse. Hence, as the compression of the bubble volume is very small (see § 3.1.2), the surface is not damaged. At the second collapse, the bubble decays into two parts, each collapsing with different violence at the left- and right-hand sides (figure 25*e*). The shock wave centres are separated by about 1550 μm. The specimen surface shows two corresponding indentations; indeed the right-hand one (at a distance of 1400 μm from the left-hand one) is poorly visible in this exposure, as it is very shallow. However, its very existence definitely proves the erosion mechanism presented here. The origin of the tiny pits appearing mainly on the right-hand side of the distinct crater is not fully understood yet. Probably, they are caused by little gas bubbles, which remain after the bubble oscillations and which are collapsed by the shock wave emitted at the moment of optical breakdown when generating the next of the 100 cavitation bubbles. As the pressure amplitude at the specimen surface (where the gas bubbles are attached) increases with decreasing initial distance, the tiny pits appear preferentially at small γ-values. Damage due to the interaction of a shock wave with gas bubbles was observed by Tomita, Shima & Sugiu (1986), Vogel *et al*. (1990), Philipp *et al*. (1993) and Bourne & Field (1995).

From about $\gamma \leqslant 0.7$, the effect of the first collapse dominates the erosion mechanism. As the jet becomes broader in the final phase of collapse, the bubble's content is compressed from 'inside' ($\gamma = 0.5$, figure 25*f*). The torus decays into multiple tiny bubbles collapsing separately. This structure of many shock wave centres along a slightly oval shape (size 1340 μm × 1400 μm) is found on the eroded specimen surface as a number of pits located along a corresponding oval circle (1200 μm × 1400 μm; compare figure 17*h*, too, where $\gamma = 0.69$).

At very small distances from the boundary ($\gamma = 0.3$, figure 25*g*), the surface is damaged seriously by the first collapse. The mechanism of a moving collapse (from both sides to the front and rear end) generates a very high pressure inside the elliptical torus formed (diameter 1130 μm × 1220 μm in figure 25*g*). Thus, after 100 cavitation bubbles, on the specimen surface a ring-shaped indentation is visible. Additionally,

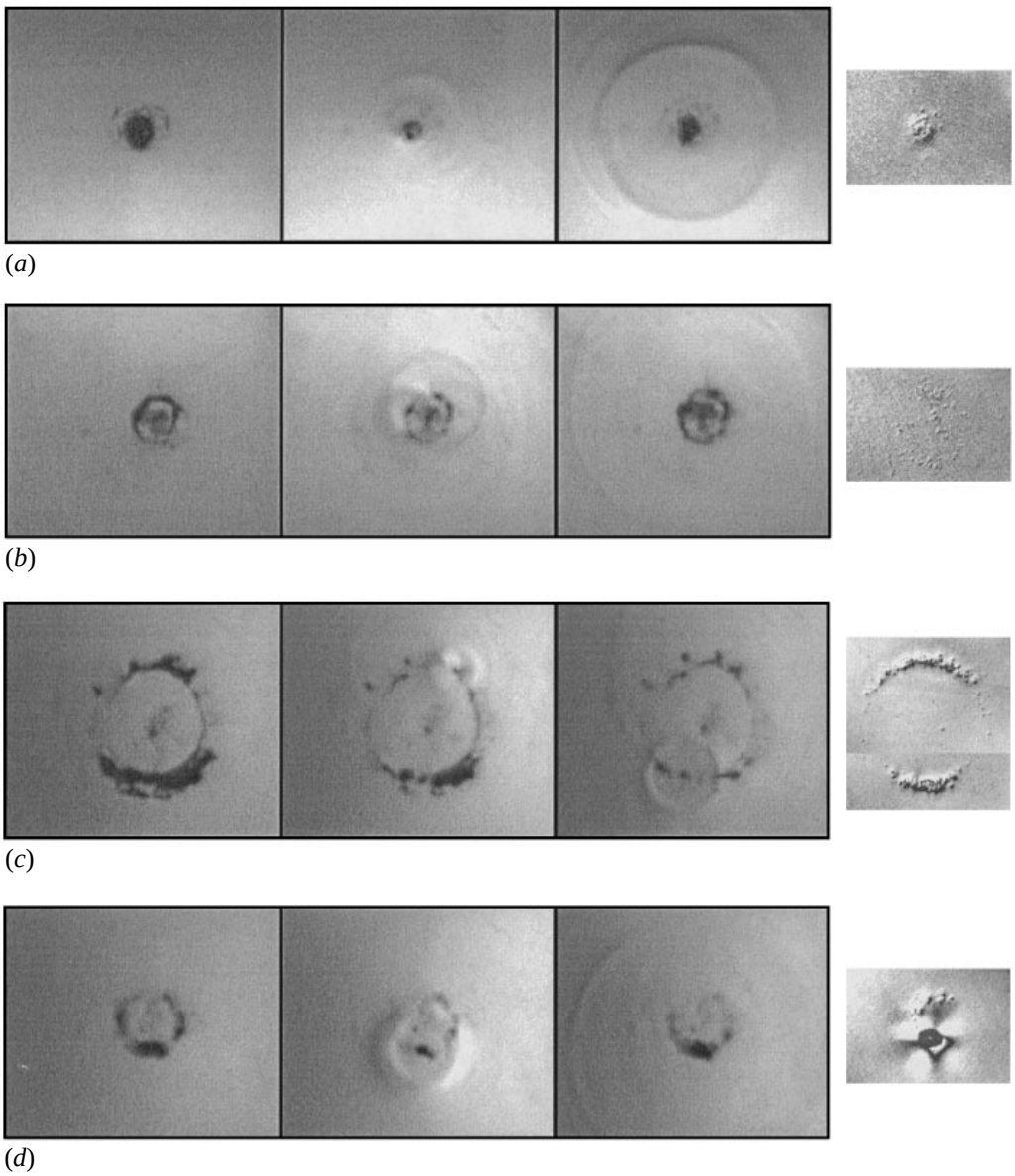

FIGURE 25 (*a–d*). For caption see facing page.

the moving shock wave further compresses the remaining part of the bubble. The maximum pressure is reached at the front and rear sides of the torus, where the compression waves from both sides reinforce. These two peak pressure regions cause the deep indentations visible in the top and bottom of figure 25(*g*). Hence, this example also shows an excellent agreement between the bubble's behaviour at the moment of collapse at the solid boundary and the structure of the resulting damage. As there is no damage observed directly underneath the plasma generated during breakdown (i.e. in the centre of the damage structure) the plasma and with it its high

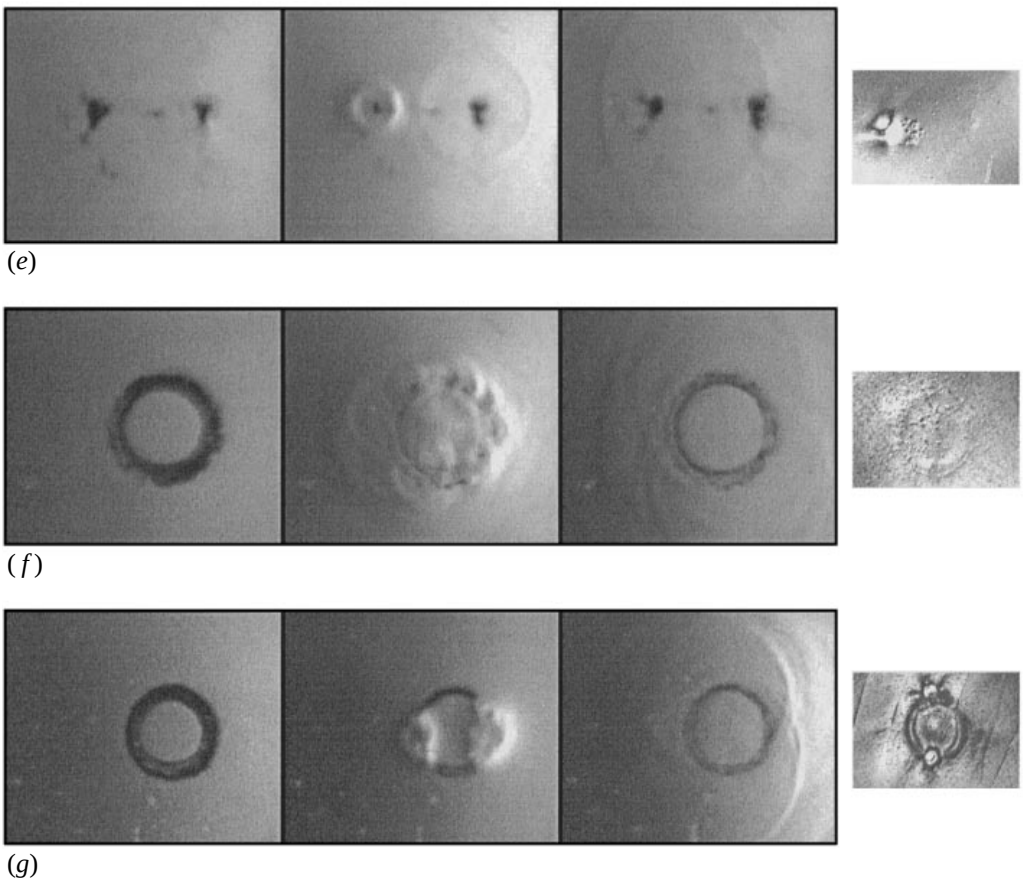

FIGURE 25. Comparison of the bubble shape at the moment of collapse (left-hand-side set of three, the collapse considered to damage is shown) with the damage pattern after the application of 100 bubbles (right-hand side) for seven different initial distances from the boundary. The pictures of bubble dynamics and damage are displayed with equal scaling and orientation (laser beam from the bottom to the top); 10^6 frames/s, frame width (left-hand side) 4.2 mm: (*a*) $\gamma = 1.9$, 2nd collapse; (*b*) $\gamma = 1.7$, 2nd collapse; (*c*) $\gamma = 1.4$, 2nd collapse; (*d*) $\gamma = 1.2$, 2nd collapse; (*e*) $\gamma = 0.9$, 2nd collapse; (*f*) $\gamma = 0.5$, 1st collapse; (*g*) $\gamma = 0.3$, 1st collapse.

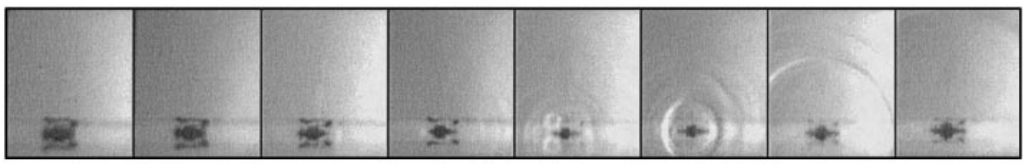

FIGURE 26. Side view of the second collapse of a bubble at $\gamma = 1.67$, $R_{max} = 1.44$ mm, 10^6 frames/s, frame width 4.0 mm. The mirror image appears in the polished surface.

temperature obviously does not reach the surface and the damage is solely due to the bubble collapse.

It should be noted that these damage patterns only occur if (nearly) identical bubbles act on the same position of a specimen. The erosion structure of real flow or acoustical cavitation is much more featureless, as the location, size and distance

of bubbles from the surface are of statistical nature, of course. Thus, the different damage patterns are superposed and could not be separated and assigned to definite bubble parameters. With the help of laser-generated bubbles it has become possible to investigate the process of erosion and its progress systematically and to determine the influence of each individual bubble with given parameters.

The erosion mechanism presented here not only shows this geometrical correlation but also a relation between the pressure acting on the boundary and the amount of damage. This amount can be expressed as the volume indented by one single cavitation bubble (see figure 21). The largest indented volumes were found in the ranges $\gamma < 0.5$ and $\gamma = 1.2$ to 1.4. The pressure emitted shows the same dependence. Vogel & Lauterborn (1988), as well as Naudé & Ellis (1961) and Tomita & Shima (1986), reported the existence of a minimum of the pressure emitted at first collapse at $\gamma = 0.9$. As the first collapse takes place in contact with the solid boundary for γ smaller than 1, the pressure load of the first collapse at the specimen surface increases with decreasing γ from $\gamma = 0.9$. This fact is in good agreement with the damage being maximum at the smallest initial distance measured ($\gamma = 0.31$). The measurements of shock wave pressure at the moment of second collapse by Vogel & Lauterborn show a maximum at $\gamma = 1.2$ to 1.5; Tomita & Shima report a maximum at about $\gamma = 1.3$. Again, the agreement with the amount of damage being caused by the second collapse for $\gamma \geqslant 1$ is remarkably good.

A quantitative estimation of the pressure acting on the solid surface is based on optical and acoustical measurements by Vogel & Lauterborn (1988). At $\gamma = 0.3$ and a maximum bubble radius of 3.5 mm, they measured a peak pressure of about $\hat{p} = 20$ MPa at a distance of 10 mm. Assuming that the proportionality between the shock wave energy E_s and the bubble energy E_b, found by Vogel & Lauterborn for the case of a spherical collapse, is also valid in the case of a collapse near a solid boundary, the pressure emitted by a bubble with $R_{max} = 1.45$ mm (this work) would be 5.3 MPa (as $E_s \sim \hat{p}^2$ and $E_b \sim R_{max}^3$, so $\hat{p}^2 \sim R_{max}^3$). At minimum volume, the cross-section of the collapsed torus has a diameter of less than 100 μm (see figure 11 *b*). Extrapolating the pressure obtained by Vogel & Lauterborn at a distance of $r = 10$ mm down to a distance of $r = 50$ μm from the emission centre inside the torus with the help of the $1/r$-law (valid for spherical, acoustic waves), the pressure at the bubble wall and thus the pressure acting on the boundary is obtained. Thus, for $R_{max} = 1.45$ mm, $\gamma = 0.31$ and $r = 50$ μm, the peak pressure is $\hat{p} = 1$ GPa. This is only a first approximation, as some factors are not considered: for example, the superposition of the waves emitted from opposing parts of the torus and the broadening of the profile due to the orbiting shock wave, which would result in a reduction of the estimated pressure. Additionally, the real thickness of the torus probably is less than 100 μm, as the shape of the torus in frame five of figure 11(*b*) is blurred due to the movement of the bubble wall during the exposure time of the camera (about 200 ns). Moreover, the shock wave amplitude following the laser-generated breakdown decreases proportional to $1/r^2$ when $r \leqslant 300$ μm (Vogel & Busch 1994) due to nonlinear effects ($\hat{p}(r = 300\ \mu\text{m}) \approx 100$ MPa). Assuming the same proportionality at the collapse-generated shock wave for distances smaller than 300 μm (where $\hat{p}(r \leqslant 300\ \mu\text{m}) \geqslant 100$ MPa), the peak pressure at $r = 50$ μm would be as high as 6.4 GPa !

When $\gamma > 1$, the second collapse induces a higher pressure at the solid boundary than the first one located farther away. The deepest pit in this γ-range was observed at $\gamma = 1.2$ (see figure 20), thus the highest pressure acts on the specimen when the bubble starts from this initial distance. The shock wave amplitude after second

collapse at $\gamma = 1.2$ and $R_{max} = 3.9$ mm is 8.3 MPa at a distance of 10 mm to the emission centre (A. Vogel 1995, personal communication). The minimum radius of the bubble, collapsed nearly hemispherically, is about 70 μm (see figure 15*b*). Thus, the calculated peak pressure of a bubble having a maximum radius of 1.45 mm is 270 MPa.

At $\gamma = 1.9$, the damage is very weak; at greater distances no damage at all was observed. This is caused by the distance of the shock wave centre from the boundary at the moment of second collapse, which rapidly increases with γ: $r = 400$ μm at $\gamma = 1.9$ (see figure 12*a*), but $r = 1500$ μm at $\gamma = 2.0$ (see figure 2*b*). For these distances, the maximum pressure at the boundary is calculated as $\hat{p}(\gamma = 1.9,\ R_{max} = 1.45\text{ mm}) = 46$ MPa and $\hat{p}(\gamma = 2.0,\ R_{max} = 1.45\text{ mm}) = 13$ MPa.

Hence, the pressure of 46 MPa is higher than the water hammer pressure of the impacting jet in the whole range of $\gamma = 1.0$ to 1.9. Owing to the circular damage, the jet could not be the cause of erosion. Thus, it can be concluded that the minimum pressure to cause a measurable plastic deformation is about 40 MPa, which is about 2.5 times the static elastic limit of aluminium (16 MPa). As the pressure at $\gamma = 2.0$ is smaller than this static limit, it is not surprising that no damage is observed for $\gamma \geqslant 2$.

4.3. *Comparison with previous results*

The basic result of this work is that cavitation erosion is mainly caused by the collapse of a bubble in contact with the material, i.e. by the high pressure (and presumingly high temperature, too) generated thereby and directly acting on the surface. This possibility was considered by several authors in the past, too. Thus, the question arises of what circumstances lead to the doubts about this mechanism.

Kornfeld & Suvorov (1944) were the first who proposed the formation of a liquid jet causing cavitation erosion. They observed a loss of stability and spherical symmetry of the bubble during collapse and concluded that Rayleigh's theory concerning a collapsing sphere is not valid for bubbles in the vicinity of a boundary. Based on their measurements that bubbles collapse down to only one third to one fifth of their maximum size, they calculated a maximum pressure of less than 2 MPa even in the case of a spherical collapse. This pressure is too low to cause the pits found by Kornfeld & Suvorov on an aluminium specimen after an experiment using acoustic cavitation. Thus, they proposed a different mechanism: due to the instabilities during the aspherical collapse the bubble surface involutes, forming a liquid flow which impacts directly onto the boundary. The availability of high-speed cameras today allows investigators to have a much closer look at the instant of collapse. It turned out that the minimum radius is much smaller than measured by Kornfeld & Suvorov. In this work, a compression ratio (R_{max}/R_{min}) of about 20 was observed ($\gamma = 1.2$: $R_{max} = 1.45$ mm, $R_{min} = 70$ μm, 10^6 frames/s), Ohl *et al*. (1995) noted as a lower limit a value of 30 ($R_{max} = 1.1$ mm, $R_{min} \leqslant 36$ μm, 2×10^7 frames/s) and Vogel *et al*. (1989) even a radius ratio of 70 ($R_{max} = 3.5$ mm, $R_{min} = 50$ μm, 10^6 frames/s). At $R_{max}/R_{min} = 30$, the pressure calculated according to Kornfeld with the Rayleigh model is 440 MPa, at $R_{max}/R_{min} = 70$ it is as high as 5.6 GPa. From his pressure measurements of spherical bubbles Vogel extrapolated a maximum pressure inside the bubble of 6 GPa.

Naudé & Ellis (1961) found a 300 μm-diameter pit after the generation of a cavitation bubble at a distance of $\gamma = 0.23$ from an aluminium specimen. As this pit diameter is much smaller than the horizontal bubble diameter at first collapse, they also concluded that the collapse could not be the cause of damage. Experimentally, they were the first who gave (indirect) evidence of the jet by visualizing the pressure

generated by the impact of the jet onto a photo-elastic material. This observation together with a calculation predicting jet velocities in the range 100 to 1000 m s^{-1} lead to the conclusion that the jet must be the cause of erosion. However, their images also show that the contrast in the photo-elastic material generated by the collapse is stronger than that generated at the moment the jet impacts onto the surface. Similar results are reported by Fujikawa & Akamatsu (1980). Thus, the collapse pressure is greater than the water hammer pressure. The pit diameter found by Naudé agrees well with the results presented in this work. Indeed, the bottom view pictures show that the diameters of the bubbles, into which the torus decays, of course are smaller than the torus diameter measured in side view by Naudé & Ellis.

A set of experiments put the jet-induced erosion mechanism into question or, at least, pointed to a smaller efficiency compared to the high pressure (and temperature) mechanism from bubble compression. Kimoto, Kamoto & Hirose (1987) registered the shock waves using four pressure sensors mounted inside the surface, but at impingement of the jet, they only detected the stagnation flow pressure and no water hammer impulse. The most important indication for a collapse-pressure/temperature damage mechanism is the observation of the circular erosion pattern on the specimen. In no way can a jet flow through the bubble centre explain a circular structure. This ring-shaped damage was not only observed by Shutler & Mesler (1965), but also by Anton & Popoviciu (1972), Shima *et al*. (1983), Tomita & Shima (1986) and Bourne & Field (1995). Tomita & Shima developed a model including the jet as well as the shock waves for causing damage. In their opinion, the jet collides with the inwardly collapsing lateral bubble walls, as at $\gamma = 1.2$, e.g., the jet hits the solid boundary at a certain instant before collapse and flows outwards radially. The collision would generate multiple tiny bubbles which would be violently collapsed by the subsequent pressure pulse emitted upon collapse of the main bubble. As the tiny bubbles are generated at the circular contact line of the bubble wall with the boundary, the damage produced should be ring shaped as well.

There are several results presented in this work which are contrary to this model. Firstly, neither Tomita & Shima nor any pictures presented here could provide evidence of the tiny bubbles predicted (see e.g. the bottom view photographs at $\gamma = 0.49$, figure 10*b*). Secondly, the question arises of why the collapse of these tiny bubbles should generate damage, but no indentation is produced by the collapse of the main bubble. Finally, at $\gamma = 1.4$ the condition that the jet must impact at the boundary before collapse is not fulfilled. The inspection of figure 2(*e*) and measurements by Tomita & Shima show that at this distance, the jet impacts not earlier than 15 μs after the moment of collapse and thus, no tiny bubbles could be generated by a collision with the bubble wall. Thus, this model can be ruled out for damage in the case of $\gamma = 1.4$. There must be another mechanism, which may consist of the second collapse of the bubble as this is toroidal. Therefore, it is conjectured that the collapse of the bubble torus in contact with the boundary causes the circular damage observed in the whole range of $\gamma = 0.3$ to 1.5.

Shutler & Mesler concluded, too, that the first and second collapse cause cavitation erosion, based on their observations with single, spark-generated bubbles above soft materials. Photographs through a transparent solid boundary showed for the first time that bubbles do collapse toroidally (for $\gamma < 1$). Additionally, they photographed the damaged surface without changing its position relative to the electrodes, i.e. the bubble centre. This enabled them to localize the position of the circular pits with regard to the bubble centre. Their exposures show that the centre of the circle is exactly below the point of bubble generation, which is also the axis of the central jet

flow. Thus, the jet could not have caused the damage. As, moreover, the diameters of the circle and the bubble torus were equal, Shutler & Mesler finally assumed as well that the pressure pulse emitted at the bubble's minimum causes the damage.

Ring-shaped damage structures were not only found in situations where a boundary causes an asymmetric collapse, but also at the interaction of a shock wave with a bubble. In a medical application of shock waves called extracorporeal shock wave lithotripsy, a focused high-pressure wave is used to disintegrate stones in the kidney or gall, for example. It is not yet known whether the destruction is caused by the shock wave alone, i.e. tension forces in its wake, or by cavitation bubbles generated in the surroundings of the stone by the stress wave accompanying the pressure wave. Experiments of Delius & Brendel (1988) have clearly shown that the rate of destruction is reduced with a reduced amount of cavitation. Also, Delius investigated the damage caused by gas bubbles on a Plexiglas specimen which are collapsed by a strong lithotripter wave (M. Delius 1991, personal communication). Again, pits around a ring were produced. This is a strong indication that the same damage mechanism as presented in this work is valid for the shock-wave-induced collapse of a bubble (Bourne & Field 1995).

5. Summary

With the combination of high-speed photography of cavitation bubble dynamics near a solid boundary and interferometric analysis of the resulting damage pattern on aluminium specimens, we were able to deduce the mechanism of cavitation erosion. The destructive effect of cavitation is mainly caused by the collapse of a bubble in contact with the solid boundary. Damage occurs when the initial bubble distance to the solid boundary is less than twice its maximum radius ($\gamma \leqslant 2$). The jetting of the bubble plays only a minor part in the erosion process; only with bubbles very close to the boundary ($\gamma \leqslant 0.7$) was additional indentation due to the impact of a jet observed. This behaviour and the various damage patterns resulting from different initial distances of the bubble from the boundary are determined by three characteristic effects of bubble dynamics:

(*a*) The translation of the bubble towards the boundary due to the asymmetric fluid flow during collapse. Thus, the bubble touches the boundary at the moment of second collapse for $\gamma \lesssim 1.9$ and at the moment of first collapse for about $\gamma \leqslant 0.9$. This explains, how the high pressures and temperatures generated upon violent collapse are able to directly act on the specimen surface. Indeed, damage was found for γ smaller than about 1.9.

(*b*) The formation of the jet, which generates a water hammer pressure upon impact onto the solid boundary. The maximum jet velocity is found to be 138 m s^{-1} at $\gamma = 3.0$. The impact velocity is smaller due to the cushioning effect of the water layer between bubble and boundary at large initial distances. At $\gamma > 1$, the impact velocity v_{imp} is smaller than 25 m s^{-1}, corresponding to a water hammer pressure p_{wh} of less than 34 MPa. At $\gamma \leqslant 1$, the jet hits the surface directly and the impact velocity increases to 83 m s^{-1} ($\gamma = 0.7$, $p_{\mathrm{wh}} = 110$ MPa). Damage from a jet was observed only with small initial distances ($\gamma \leqslant 0.7$).

(*c*) The formation of a ring vortex. This effect influences the shape of the bubble at the moment of a boundary-contact collapse and thus determines the structure of the damage. A good agreement between the locations of shock wave emission centres on the ring and the damage pattern was found. For example, at $\gamma = 1.9$, the second collapse proceeds nearly hemispherically with the bubble collapsing to a single point.

Accordingly, one indentation was found on the specimen directly below the bubble centre. When γ is smaller than about 1.7, a bubble torus is formed due to the jet flow through the bubble centre, which decays into several microbubbles along the torus ring during second collapse. The shock waves emitted upon collapse of these microbubbles were visualized by bottom-view shadowgraph exposures of the bubble. In analogy to that structure of pressure centres, the pits produced by the cavitation bubble were found to be located on the circumference of a circle. For γ-values smaller than about 0.7, the effect of the first collapse dominates the erosion mechanism. The bubble shape is toroidal again, but this time, the torus collapses from the inner side. Again torus size and damage ring size coincide. Thus the equality in size of the bubble torus at collapse and of the damage ring produced observed for all γ can be considered as final proof for the contact damage mechanism.

An estimation of the peak pressure at the solid boundary reveals a pressure of more than 1 GPa at $\gamma = 0.3$. At the greatest initial distance where damage was observed ($\gamma = 1.9$), the estimated peak pressure acting on the boundary is 46 MPa. This shock-wave-induced load is higher than the water hammer pressure induced by the jet impact at $\gamma > 1$.

One single bubble can produce pits with a maximum depth of 8 μm (at $R_{max} =$ 1.45 mm; typical value: 2 μm) and a maximum pit diameter of 570 μm (typical 250 μm). A scaling value for the damage potential of a bubble is the indented volume. The largest damage volumes generated by one single bubble were found with bubbles in the range $\gamma \leqslant 0.3$ and $\gamma = 1.2$ to 1.4. At fixed γ-values, the diameter of the damaged area is proportional to the maximum bubble radius.

Not only soft aluminium specimens could be damaged by laser-generated cavitation bubbles. Though no damage was observable after the exposure of harder materials to only one single bubble, 100 bubbles produced measurable indentations on the tested materials, brass, mild steel and duplex steel. It was found that the maximum indentation depth after the exposure of mild steel to 100 bubbles was only 1/100 of the depth on aluminium, whereas the yield strength of mild steel is greater by a factor of 15. As a high number of identical bubbles could be generated in a short time interval (for example 5000 bubbles in about 15 minutes), this technique can be used to test the erosion resistance of even very hard materials.

The authors would like to thank Dr-Ing. Manfred Feyer for the supply of highly polished specimens and the company Atos GmbH for the allowing use of their interference microscope Micromap 512. Thanks are also due to Dr Michael Delius for his careful proof reading of the manuscript and to Dr Alfred Vogel for valuable discussions and for provision of data from his pressure measurements. Further thanks go to C.-D. Ohl for help with the manuscript. We acknowledge the financial support from the Deutsche Forschungsgemeinschaft and the Fraunhofer Gesellschaft for loan of equipment.

REFERENCES

Anton, I. & Popoviciu, M. 1972 The behavior of hemispherical bubbles generated by electric sparks. In *Proc. 4th Conf. Fluid Machinery*, p. 89.

Benjamin, T. B. & Ellis, A. T. 1966 The collapse of cavitation bubbles and the pressure thereby produced against solid boundaries. *Phil. Trans. R. Soc. Lond.* A **260**, 221–240.

Blake, J. R. & Gibson, D. C. 1987 Cavitation bubbles near boundaries. *Ann. Rev. Fluid Mech.* **19**, 99–123.

Blake, J. R., Taib, B. B. & Doherty, G. 1986 Transient cavities near boundaries. Part 1. Rigid boundary. *J. Fluid Mech.* **170**, 479–497.

Bourne, N. K. & Field, J. E. 1992 Shock-induced collapse of single cavities in liquids. *J. Fluid Mech.* **244**, 225–240.

Bourne, N. K. & Field, J. E. 1994 Cavity collapse in a liquid with solid particles. *J. Fluid Mech.* **259**, 149–165.

Bourne, N. K. & Field, J. E. 1995 A high-speed photographic study of cavitation damage. *J. Appl. Phys.* **78**, 4423–4427.

Brunton, J. H. 1970 Cavitation Damage. In *Proc. 3rd Intl Conf. Rain Erosion and Associated Phenomena* (ed. A. A. Fyall & R. B. King), pp. 821–843. Royal Aircraft Establishment.

Cook, S. S. 1928 Erosion by water-hammer. *Proc. R. Soc. Lond.* A **119**, 481–488.

Dear, J. P., Field, J. E. & Walton, A. J. 1988 Gas compression and jet formation in cavities collapsed by a shock wave. *Nature* **332**, 505–508.

Delius, M. 1990 Effect of lithotripter schock waves on tissues and materials. In *Proc. 12th ISNA: Frontiers of Nonlinear Acoustics* (ed. M. F. Hamilton & D. T. Blackstock), pp. 31–46. Elsevier.

Delius, M. & Brendel, W. 1988 A mechanism of gallstone destruction by extracorporeal shock waves. *Naturwissenschaften* **75**, 200–201.

Domke, W. 1987 *Werkstoffkunde und Werkstoffprüfung*. Cornelsen.

Field, J. E. 1994 Experimental studies of cavity collapse. In *Proc. IUTAM Symp. 'Bubble Dynamics and Interface Phenomena'* (ed. J. R. Blake *et al.*), pp. 17–31. Kluwer.

Fujikawa, S. & Akamatsu, T. 1980 Effects of the non-equilibrium condensation of vapour on the pressure wave produced by the collapse of a bubble in a liquid. *J. Fluid Mech.* **97**, 481–512.

Gibson, D. C. 1968 Cavitation adjacent to plane boundaries. In *Proc. Third Australasian Conference on Hydraulics and Fluid Mechanics*. The Australian Institution of Engineers.

Güth, W. 1954 Kinematographische Aufnahmen von Wasserdampfblasen. *Acustica* **4**, 445–455.

Haller, P. de 1933 Untersuchungen über die durch Kavitation hervorgerufenen Korrosionen. *Schweiz. Bauzeit*. **101**, 243–246.

Hariharan, P., Oreb, B. F. & Eiju, T. 1987 Digital phase–shifting interferometry: a simple error–compensating phase calculation algorithm. *Appl. Opt*. **26**, 2504–2505.

Harrison, M. 1952 An experimental study of single bubble cavitation noise. *J. Acoust. Soc. Am.* **24**, 776–782.

Hornbogen, E. 1983 *Werkstoffe*. Springer.

Ihler, B. C. & Hirth, A. 1991 Experimental investigation of acoustic and cavitation processes generated by the laser – lithotripsy. *J. Phys.* **1**, 203–206.

Jones, I. R. & Edwards, D. H. 1960 An experimental study of the forces generated by the collapse of transient cavities in water. *J. Fluid Mech.* **7**, 596–609.

Jungnickel, K. 1995 Experimentelle Untersuchungen zur Kavitationsblasendynamik und ihrer Rolle bei der Disruption und Fragmentierung von biologischem Material. PhD thesis, Lübeck.

Kimoto, H., Kamoto, A. & Hirose, T. 1987 A study on impulsive pressure of a collapsing cavitation bubble. *JSME Intl J.* **30**, 449.

Kling, C. L. & Hammitt, F. G. 1972 A photographic study of spark–induced cavitation bubble collapse. *Trans. ASME* D: *J. Basic Engng* **94**, 825–833.

Kornfeld, M. & Suvorov, L. 1944 On the destructive action of cavitation. *J. Appl. Phys.* **15**, 495–506.

Lauterborn, W. 1974 Kavitation durch Laserlicht. *Acustica* **31**, 51–78.

Lauterborn, W. 1982 Cavitation bubble dynamics – new tools for an intricate problem. *Appl. Sci. Res.* **38**, 165–178.

Lauterborn, W. & Bolle, H. 1975 Experimental investigations of cavitation–bubble collapse in the neighbourhood of a solid boundary. *J. Fluid Mech.* **72**, 391–399.

Lush, P. A. 1983 Impact of a liquid mass on a perfectly plastic solid. *J. Fluid Mech.* **135**, 373–387.

Naudé, C. F. & Ellis, A. T. 1961 On the mechanism of cavitation damage by nonhemispherical cavities collapsing in contact with a solid boundary. *Trans. ASME* D: *J. Basic Engng* **83**, 648–656.

Ohl, C. D., Philipp, A. & Lauterborn, W. 1995 Cavitation bubble collapse studied at 20 million frames per second. *Ann. Physik* **4**, 26–34.

PHILIPP, A., DELIUS, M., SCHEFFCZYK, C., VOGEL, A. & LAUTERBORN, W. 1993 Interaction of lithotripter–generated shock waves with air bubbles. *J. Acoust. Soc. Am.* **93**, 2496–2509.

PHILIPP, A. & LAUTERBORN, W. 1997 Damage of solid surfaces by single laser–produced cavitation bubbles. *Acustica* **83**, 223–227.

PLESSET, M. S. & CHAPMAN, R. B. 1971 Collapse of an initially spherical vapour cavity in the neighbourhood of a solid boundary. *J. Fluid Mech.* **47**, 283–290.

RAYLEIGH, LORD 1917 On the pressure developed in a liquid during the collapse of a spherical cavity. *Phil. Mag.* **34**, 94–98.

SHIMA, A., TAKAYAMA, K., TOMITA, Y. & MIURA, N. 1981 An experimental study on effects of a solid wall on the motion of bubbles and shock waves in bubble collapse. *Acustica* **48**, 293–301.

SHIMA, A., TAKAYAMA, K., TOMITA, Y. & OHSAWA, N. 1983 Mechanism of impact pressure generation from spark-generated bubble collapse near a wall. *AIAA J.* **21**, 55–59.

SHUTLER, N. D. & MESLER, R. B. 1965 A photographic study of the dynamics and damage capabilities of bubbles collapsing near solid boundaries. *Trans. ASME* D: *J. Basic Engng* **87**, 511–517.

SILBERRAD, D. 1912 Propeller erosion. *Engineering*, 33–35.

STEINBERG, D. J. 1993 A brief review on cavitation bubble collapse near a rigid boundary. *J. Stone Dis.* **5**, 49–59.

STRASBERG, M. 1953 The pulsation frequency of nonspherical gas bubbles in liquids. *J. Acoust. Soc. Am.* **25**, 536–537.

TOLANSKY, S. 1973 *An Introduction to Interferometry*. Longman.

TOMITA, Y. & SHIMA, A. 1986 Mechanisms of impulsive pressure generation and damage pit formation by bubble collapse. *J. Fluid Mech.* **169**, 535–564.

TOMITA, Y., SHIMA, A. & SUGIU, T. 1986 Mechanisms of impulsive pressure generation and damage pit formation by bubble–shock wave interaction. In *Proc. Intl Symp. Cavitation, Sendia, Japan, 16–19 April 1986* (ed. H. Murai), pp. 77–82.

VOGEL, A. & BUSCH, S. 1994 Time-resolved measurements of shock-wave emission and cavitation-bubble generation in intraocular laser surgery with ps– and ns–pulses. In *Proc. IUTAM Symp. 'Bubble Dynamics and Interface Phenomena'* (ed. J. R. Blake *et al.*), pp. 105–117. Kluwer.

VOGEL, A. & LAUTERBORN, W. 1988 Acoustic transient generation by laser–produced cavitation bubbles near solid boundaries. *J. Acoust. Soc. Am.* **84**, 719–731.

VOGEL, A., LAUTERBORN, W. & TIMM, R. 1989 Optical and acoustic investigations of the dynamics of laser–produced cavitation bubbles near a solid boundary. *J. Fluid Mech.* **206**, 299–338.

VOGEL, A., SCHWEIGER, P., FRIESER, A., ASIYO, M. & BIRNGRUBER, R. 1990 Intraocular Nd:YAG laser surgery: damage mechanism, damage range and reduction of collateral effects. *IEEE J. Quant. Electr.* **26**, 2240–2260.

VOINOV, O. V. & VOINOV, V. V. 1976 On the process of collapse of a cavitation bubble near a wall and the formation of a cumulative jet. *Sov. Phys. Dokl.* **21**, 133–135.

WARD, B. & EMMONY, D. C. 1991*a* Interferometric studies of the pressures developed in a liquid during infrared-laser-induced cavitation-bubble oscillation. *Infrared Phys.* **32**, 489–515.

WARD, B. & EMMONY, D. C. 1991*b* Direct observations of the pressure developed in a liquid during cavitation–bubble collapse. *Appl. Phys. Lett.* **59**, 2228–2230.

ZHANG, S., DUNCAN, J. H. & CHAHINE, G. L. 1993 The final stage of the collapse of a cavitation bubble near a rigid wall. *J. Fluid Mech.* **257**, 147–181.